A case study of a West Sumatra squall line using satellite observations

Clemente Lopez-Bravo*, Claire L. Vincent, Yi Huang and Todd Lane

School of Geography, Earth and Atmospheric Sciences, and ARC Centre of Excellence for Climate Extremes, The University of Melbourne, Melbourne, Victoria, Australia

Corresponding author: Clemente Lopez-Bravo, llopezbravo@student.unimelb.edu.au

ABSTRACT

A West Sumatra squall line occurred on 10 January 2016, with a clear offshore propagation of convection. Satellite-derived products from Himawari-8 Advanced Himawari Imager and the Geostationary Cloud Algorithm Testbed Geocat are used to investigate the westward propagation of cloudiness from Sumatra to the Indian Ocean with a lifetime of 1.5-days. A convective mask based on deep convective cells detection and a cell-tracking algorithm are used to estimate the propagation speed of the cloud system. Two distinct mesoscale convective responses are identified: (1) a rapid development in South Sumatra is influenced by the convective environment over the Indian Ocean. The propagation speed is estimated to be ~5 m s^{-1} within the first 200 km from the coast. This speed is consistent with density currents. In contrast, (2) the coupling to the inertia-gravity wave is only evident for the northwest of Sumatra with speed ~12 m s^{-1}. The analysis of brightness temperature from the 10.4 μm spectral band and cloud top temperature showed that the lifetime of the squall line is approximately 30 h with a propagating distance of ~1000 km. Retrieved cloud properties and tracking of the offshore propagation indicated that the cloud structure consisted of multiple types of cells, propagating as envelopes of convection and revealed the influence of large-scale variability of the Indian Ocean. Filtered OLR anomalies, satellite-derived rainfall, moisture flux convergence, and background winds flow around Sumatra are used to explore the effects of Kelvin wave activity that likely influenced the lifetime of the squall line.

1. Introduction

Analysis of the multi-scale variability of diurnally forced convection in the Maritime Continent (MC) requires well-resolved data in space and time, which also has broad spatial coverage. While previous studies have established the climatological characteristics of these convective systems, there are gaps in the detailed understanding of the processes behind their evolution. This is, in part, due to the limited spatiotemporal resolution (McGarry and Reed 1978; Albright et al. 1981; Chen and Houze 1997; Short et al. 2019) and spatial coverage of the satellite datasets used, or the inherent limitations of model simulations (Yang and Slingo 2001; Love et al. 2011; Vincent and Lane 2016, 2017). The advent of new-generation geostationary satellites, such as Himawari-8, with revolutionary spatiotemporal and spectral resolutions, provide opportunities to investigate tropical convection in unprecedented detail. This study uses geostationary data with high spatial and temporal resolution and broad spatial coverage to examine the diurnal and topographically-forced convection over Sumatra that evolves to a long-lived squall line interacting with intra-seasonal variability over the Indian Ocean (IO) and the cloud features of the offshore-propagating squall line northwest of Sumatra. The goal of this work is to explore the diurnally forced convection in the MC, using the Himawari-8 Advanced Himawari Imager (AHI) data and satellite-derived cloud properties. The study investigates the signatures of diurnally driven convection over Sumatra and the eastern IO in January 2016, and the influence of the moist Kelvin wave propagation on the longevity of the Mesoscale Convective Systems (MCS) ahead of the Kelvin wave propagation over the Maritime Continent.

Previous studies in the tropics have found a rainfall maximum over the sea in the early morning, while over the land, the maximum is observed in the late afternoon or during the evening. The observed atmospheric patterns, however, differ across geographical locations and through the

tropics. Yang and Slingo (2001) used satellite observations and atmospheric modeling to explain that precipitation over the land often propagates in a seaward direction during the afternoon and evening. At night and during the early morning, the precipitation is located offshore in areas such as the Bay of Bengal, northeast of New Guinea, Mexico, and West of the African coast. Studies have used satellite-based datasets and numerical atmospheric models to investigate the evolution of the DC over the equatorial region (Yang and Slingo 2001) and the tropical Americas (Mapes et al. 2003). They observed that the triggering of MCSs over tropical oceans resulted from interactions between the diurnal heating cycle, the planetary boundary layer, and topographic effects. Mapes et al. (2003) showed that mesoscale convective systems associated with coastal and continental regimes propagate with an average horizontal phase velocity between 2-8 m s^{-1} near the coast, and 11 and 20 m s^{-1} farther offshore. The ranges of speed depend on the region and the type of local forcing. Observational and numerical modeling studies have shown evidence of slower propagation near shore regime linked to cold pools and land breeze density currents with a range of speeds of approximately 2–8 m s^{-1} (Houze et al. 1981; Sakurai et al. 2009; Fujita et al. 2011; Vincent and Lane 2016; Short et al. 2019; Ruppert and Zhang 2019; Ruppert et al. 2020). The faster propagation offshore is found between 11 and 20 m s^{-1} to be a response to the intense stratiform heating structure in the organized convection that develops higher-order gravity waves (Mapes et al. 2006; Tulich et al. 2007; Tulich and Mapes 2008; Love et al. 2011; Vincent and Lane 2016; Ruppert et al. 2020) although that speed may be lower in some regions such as the Maritime Continent, where vertical wavelengths are smaller than the depth of the troposphere and the phase speed is in the range of approximately 11–20 m s^{-1}.

Similar results were found by Mori et al. (2004) for Sumatra, where Tropical Rainfall Measuring Mission (TRMM) satellite precipitation radar and sounding data were used to explore the regional variability of rainfall. Spatial and temporal rainfall patterns were found to be driven by the

migration of the daytime rainfall peak over the land to the offshore region at night, with a typical propagation distance of around 400 km. Two propagation speeds were reported; (1) approximately 10 m s^{-1} for the first 100 km and (2) approximately 30 m s^{-1} farther offshore. They found that the contribution of convective rainfall varied with proximity from the coast, with up to 70% of evening rainfall explained by convective processes. Thus, the weather systems in South Sumatra may be interpreted as a dynamical response of the diurnally driven convection over Sumatra to local forcings such as mountains and the effects of background westerly wind during the austral summer, feedback processes involving local convergence and thermal heating associated with the land- and sea-breezes, as well as the interconnection with the diurnally driven convection over Java, Borneo, and the Malay Peninsula.

Rainfall in the MC has diverse sources of variability with distinct spatial- and time-scales. On the intraseasonal scale, the dominant source of variability in the tropics is the Madden-Julian Oscillation (MJO) on time-scales of 30-70 days with an eastward propagation speed of approximately 5 m s^{-1}. The propagation creates areas of enhanced or suppressed convection starting over the IO and propagating through the tropics towards the western Pacific Ocean. Frictional moisture convergence associated with Kelvin wave activity ahead of the MJO, changes in solar insolation and modulation of the background winds have been invoked to explain the variations in the diurnally driven convection over land and coastal areas of the MC, along with the MJO itself (Peatman et al. 2014; Birch et al. 2016; Rauniyar and Walsh 2013; Short et al. 2019). The interaction between topography and Kelvin waves can generate changes in the frictional moisture convergence when the system propagates towards the MC; this has been argued to amplify the signature of the DC over the land (Takayabu and Murakami 1991; Serra et al. 2014; Peatman et al. 2014). In contrast, when the MJO is convectively suppressed near the MC, the frictional moisture divergence and reduced solar insolation can substantially suppress the signature of the DC over the land. Chen et al. (1996) used

infrared satellite imagery to show that the pattern of cold cloud shields with westward propagation behave like an equatorial internal gravity wave but with a 2-day frequency. A possible explanation is that the lifetime increases due to the reinforcement of the DC of the marine planetary boundary layer associated with the effects between individual MCSs and 2-day waves in the tropics, despite the differences in time-scale between them (Takayabu 1994; Chen and Houze 1997; Mapes et al. 2006).

The influence of the MJO on the diurnal precipitation cycle over the MC has been explored in several studies (e.g., Rauniyar and Walsh 2011; Peatman et al. 2015; Birch et al. 2016; Hassim et al. 2016; Vincent and Lane 2016; Ruppert and Zhang 2019; Seiki et al. 2021a). Convective-permitting simulations using the Weather Research and Forecasting (WRF) Model together with satellite-derived rainfall TRMM and CMORPH were employed to explore the processes associated with the seaward-propagating precipitation in New Guinea (Vincent and Lane 2016). Based on previous investigations (Yang and Slingo 2001; Mapes et al. 2003; Love et al. 2011), two propagation speeds were found: the first was situated within 100-200 km from the coast the propagation was on average 4 m s^{-1}. The second was found between 400 and 700 km, where the speed falls in the range of 12-18 m s^{-1}. The latter is consistent with the propagation of an IGW as a response of the DC of heating and cooling over land, as proposed in several studies (Rotunno 1983; Weisman and Rotunno 2004; Yang and Slingo 2001; Mapes et al. 2003; Qian 2008). These studies also found significant differences between WRF simulations and satellite-based rainfall estimates, which were associated with uncertainties in satellite retrievals, model biases in the representation of convection, and challenges in capturing the interscale cloud feedback components in global and limited-area models over the Indo-Pacific warm pool (Vincent and Lane 2016, 2017).

Recent studies have explored the effect of surface winds across the MC on rainfall processes. Short et al. (2019) used two satellite-based rainfall and three satellite-based sea surface wind

datasets to investigate the links between the DC of surface winds and offshore rainfall associated with MCSs. The observational analysis of the land-sea breeze showed an average propagation distance of around 400 km from the coast, and wind disturbances were related to propagation offshore of rainfall with a range of speeds between 1 and 5 m s^{-1} near the coast and 25-30 m s^{-1} farther offshore, corresponding with gravity wave propagation. These results are comparable with the speeds found using numerical simulations (Hassim et al. 2016; Vincent and Lane 2016). However, three main components of the DC of rainfall were identified: two are associated with the land-sea breeze processes, whereas the contribution of the open ocean DC 400-800 km offshore from South Sumatra describes the third one. These findings show the critical location of Sumatra, where the IO and the MC meet and define the dynamical and thermodynamic conditions necessary for convective initiation and MCSs development in a tropical atmosphere.

Capitalizing on the atmospheric and cloud properties derived from the Himawari-8 satellite, this study aims to explore the diurnally driven convection associated with a tropical squall line event in Sumatra to further our understanding of the lifetime, structure and variability of tropical mesoscale convective systems and the underlying processes. We employ the atmospheric and cloud products derived from the Himawari-8 satellite, which provide higher-resolution data over a broader spatial area than previously used to study the cloud features in the region. At this resolution the mean propagation of the cloud system that has been previously reported (e.g., Mori et al. 2004) to be perpendicular to the coastline is better defined as envelopes of convection rather than squall lines themselves. However, the brightness temperature (BT) 10.4 μm spectral band, cloud top temperature (CTT), cell-tracking, and convective mask show a meridional transition between the northwest and southwest of Sumatra. The northwestern line shows slow, fast, and transition speed components of the propagation and cloudiness signatures of the diurnally driven convection over Sumatra and the eastern IO that links to density currents and IGW mechanisms. In contrast, the

southwestern line shifts to a slow propagation dominated by a density current due to the weather conditions during the squall line event. This squall line event, occurring on 10-11 January 2016, is chosen as it features a clear offshore land/sea breeze (Fig. 1) and the effect of the convection over the eastern IO on the lifetime of the squall line. Moreover, the event occurs under suppressed MJO and Kelvin wave activity over the MC, therefore exemplifying local forcing effects. Using a range of satellite-based and reanalysis datasets including the unprecedented high-resolution Himawari-8 AHI products, this study aims to address the science questions as follows: (1) what are the characteristics of the diurnally driven convection over the North and South Sumatra? (2) how do these responses evolve under different local and large-scale forcings? (3) what are the sources of the different responses? The remainder of this paper is organized as follows: Section 2 describes the characteristics of satellite-derived cloud properties from Himawari-8 AHI. The propagation of the squall line is analyzed in section 3, focusing on the cloud structure and properties over the West coast of Sumatra (WCS). Discussion and conclusion are presented in sections 4 and 5.

2. Data and Methodology

a. The satellite-derived dataset from Himawari-8

The atmospheric and cloud products derived from Himawari-8 AHI were produced employing the Community Satellite Processing Package for Geostationary Data, Geostationary Cloud Algorithm Testbed (CSPP-Geo Geocat) Level-2 version 1.0.3. in conjunction with additional ancillary datasets as presented in Table 1. Himawari-8 AHI data was provided by the Japanese Meteorological Agency. Two databases were produced with the CSPP-Geo Geocat at the same spatial resolution (2-km) but different temporal resolutions: 1-hour (Lopez-Bravo et al. 2021a,b) and 10-minute, respectively. The hourly dataset was employed to characterize large-scale drivers over the MC

during the austral summer from November 2015 to March 2016, and the 10-minute dataset was used to investigate the evolution, and the internal structure of the squall line event from 07:00 LST 10 January 2016 to 06:50 LST 14 January 2016. Retrieved CTT and cloud top height (CTH) were employed to examine the squall line propagation and the diurnally driven convection over Sumatra. These retrieved cloud properties have previously been found to agree reasonably well with the estimates from the Cloud-Aerosol Lidar and Infrared Pathfinder Satellite Observation (CALIPSO) and shipborne cloud radar-lidar observations (Huang et al. 2019).

A multi-threshold post-processing method was further implemented to remove pixels that may be subject to significant uncertainties and retrieval artifacts. Sun glint, for example, can sometimes lead to misclassification of the water surface as a cloud scene, resulting in false cloud detection. Based on the analysis in Huang et al. (2019), a number of threshold values were carefully chosen and used to filter out pixels that are deemed unreliable (Table 2). While the filtered dataset may under-represent the fraction of very shallow and partly cloudy pixels to some extent, it minimizes the systematic retrieval errors, which may otherwise lead to poor interpretation of the results.

b. Convection Identification and Masking

Based on the concept that deep convection penetrates the tropical tropopause layer and changes water vapor content in the lower stratosphere, the overshooting cloud tops are used as a proxy of thunderstorm updrafts embedded in the squall line. The overshooting cloud tops as part of the squall line modifies the static stability near the tropopause and generates gravity waves. These processes can promote turbulence and mixing, which promotes mass exchange between the troposphere and stratosphere (e.g., Hassim and Lane 2010). Specifically, the overshooting convection will transport water vapor into the upper-troposphere and lower-stratosphere and can generate extensive regions of large ice water content with very low BT. A combination of techniques was used to identify

and classify deep convective areas of the squall line structure, following Mecikalski and Bedka (2006), Walker et al. (2012), and Merk and Zinner (2013). The gradient technique was used to estimate the intensity gradient of brightness at a pixel level in the zonal and meridional direction to identify the immature and mature regions during the daytime. In order to avoid the problem of nighttime identification, a threshold technique based on the brightness temperature difference between the 10.4 μm and 12.4 μm spectral bands (BT difference < 3.5 K) was used to define the outer limit of the immature region. The threshold technique performed well in detection due to well-organized deep tropical convection without a significant cover of intermediate, low, and thin clouds. The next brightness threshold technique was applied to identify a deep convective cloud scene using BT from channel 13 (10.4 μm spectral band) and channels 8 (6.2 μm spectral band). Thresholds have been selected from the literature because long-term statistics of cloud BT derived from Himawari-8 AHI over Sumatra are not available. BT thresholds that have been used in the literature to identify deep convection include BT < 241 K (Maddox 1980), BT < 245 K (Machado et al. 1993; Mapes and Houze Jr. 1992) and BT < 235 (Vila et al. 2008). In this study, $BT_{10.4\mu m}$ > 253 K was chosen to separate immature and mature convective regions based on Roberts and Rutledge (2003), whereas $BT_{10.4\mu m}$ < 213 K (modified by Takayabu (1994) for the MC) was chosen to indicate deep convection. Those conditions have to include the high-water signature at troposphere level, which can be estimated by the BT difference between 6.2 μm and 10.4 μm channels. In this study $BT_{6.2\mu m}$-$BT_{10.4\mu m}$> -10 K is chosen to indicate pixels with mature cumulus class, while values greater than -10 K are classified as immature clouds. Together, these thresholds provide a convective cloud mask with three categories: deep convection (M_DC), mature (M), and immature (IM).

Additionally, cold cloud cores associated with deep convective clouds of the squall line were identified using the brightness temperature (10.4 μm spectral band) from Himawari-8 AHI following Moseley et al. (2013, 2016), Feng et al. (2018).

c. Tracking of cloud cells

A cell-tracking algorithm was developed based on the convective cloud-mask to characterize the behavior and evolution of the deep convective clouds. This algorithm uses the deep convective cloud from the convective mask and the BT channel 13 to identify the center of the target. The center of the target is determined via a two-stage approach. Firstly, the data is restricted to the coldest 5^{th} percentile of the BT (10.4 μm) to reduce the search area over the target. Then, the coldest 1^{st} percentile of the BT is used to identify the coldest region of the target. When all the coldest pixels are found, the geometric midpoint is assigned as the center of the target. Once identified, a correlation method based on Sum of Squared Differences is used to track the cloud between the target scene, at some time t, in a search scene forwards or backwards in time, generating the displacement and new deep convective cell position in time and space. The lifetime of the cell is calculated as a function of cloud cover/number of pixels every 10-minutes during the squall line evolution in each category of the convective mask. This methodology is similar to that used in Williams and Houze (1987), Johnson et al. (1998) and Vila et al. (2008). In this study, convective initiation is not incorporated in the algorithm because the squall line was selected by manual inspection.

Apart from Himawari-8 AHI products, additional information is used to analyze the large-scale environment and squall line evolution. Interpolated Outgoing Long-wave Radiation (OLR) data was obtained from the Earth System Research Laboratory/Physical Sciences Division (Liebmann and Smith 1996). Time indices of Kelvin waves were obtained by first filtering OLR data in the

wavenumber-frequency domain with wave numbers 1-14, a period of 2.5-20 days and equivalent depth of 8-90 m (Wheeler and Kiladis 1999; Kiladis et al. 2006). ERA5 zonal and meridional wind components are used to show the low- and mid-level background wind during the squall line event, and the daily accumulated rainfall is calculated by using the Integrated Multi-satellitE Retrievals for Global Precipitation Measurement (IMERG) (Huffman et al. 2015). The propagation of the atmospheric disturbances associated with the diurnally driven convection and cloud properties from Indonesia toward the IO were explored using satellite-derived Level-1 (Lopez-Bravo et al. 2021a) and Level-2 (Lopez-Bravo et al. 2021b) cloud properties derived from Himawari-8 AHI. Reflectivity from the Cloud Profiling Radar onboard the CloudSat satellite (Stephens et al. 2002) was employed to explore the vertical structure of clouds associated with the squall line at 14:25 LST 11 January 2016.

3. Results

a. Influence of the large-scale mechanisms on squall line event

Zonal and meridional wind components from ERA5 were vertically averaged over the 925-850 hPa layer and at 700 hPa to show the synoptic background wind during the squall line event from 10 January 2016 to 12 January 2016. A Low-level easterly flow regime was identified over the MC. The maximum speed of approximately 8 m s^{-1} was located at longitude 111°E, and latitudes between 5°N and 10°N. For the Malay Peninsula, easterly flow was directed around the mountains to the South, impinging on the Central and South Sumatra (Fig. 2a). Easterly flow crossed the narrow island gap towards the Strait of Malacca and skirted the Northern region of Sumatra. As a result, a low-speed area was located between the North of Sumatra and the IO. In contrast, the easterly flow over the Java Sea is weak near Sumatra but intensifies over the Southern IO.

Finally, the anticyclonic circulation over the Bay of Bengal contributed to southeasterly flow towards the equator over the IO. The mid-level wind field at 700 hPa (Fig. 2b) showed that the easterly flow from the MC modified the flow over Sumatra to acquire a southeasterly direction, and a cyclonic circulation dominated in the Southern IO. A relative vorticity analysis was performed to understand the circulation induced by the mountains of the Malay Peninsula and the mountain range on the Western side of Sumatra (Barisan Mountains with an average elevation of 2,400 m above sea level). The split flow near the Malay Peninsula can be approximated by a stratified flow being blocked by an isolated obstacle (Smolarkiewicz and Rotunno 1989; Rotunno and Smolarkiewicz 1991; Fine et al. 2016). The potential for flow blocking may be indicated by the Froude number, defined by U/Nh, where U is the approaching wind speed, N is the Brunt–Väisälä frequency, and h is the obstacle height. A Froude number < 1 can indicate flow blocking (Smolarkiewicz and Rotunno 1989). The average Froude number at the low-level layer (925-850 hPa) was 0.4; this supports the flow blocking and splitting by the high mountains of the Malay Peninsula and Sumatra. Relative vorticity and streamlines (925-850 hPa layer) are shown in Fig. 2c. A positive vorticity maximum is observed at the northern region of Sumatra, consistent with a cyclonic circulation over the IO. The maximum relative vorticity propagates offshore from the northern region of Sumatra during the squall line event, extending towards the equator and the longitude 90°E. However, cyclonic or negative values of relative vorticity (Southern Hemisphere) are also found over the South of Sumatra with a closed offshore circulation extending into a wide area of negative vorticity over most of the Southern IO (Latitude between equator and 10°S). This vast region reflects the existence of a regional circulation over the Southern IO, evident in the 700 hPa analysis and also at lower levels on individual days (not shown).

The period of December 2015-February 2016 was analyzed using the Wheeler and Hendon (2004) real-time multivariate MJO index (WH04) to identify the MJO phase under which the

squall line event occurred. The WH04 index is based on the first two principal components of OLR, and the 850-hPa and 200-hPa zonal wind from NCEP reanalysis averaged over 15°S-15°N. Between 9 January 2016, and 13 January 2016, the MJO was active over the Western Hemisphere and the IO and weakened as it approached the MC at the end of January (Fig. 2d). Suppressed convection over the MC was associated with the eastward propagation of the MJO from Africa towards the IO. The transition to phase 2 occurred in late January, a few days after the squall line event, without evidence of the atmospheric disturbances traveling eastward over the IO. Although the enhanced convective phase of the MJO had not yet arrived at Sumatra on 10 January 2016, the diurnally driven convection over Sumatra appeared to be influenced by non-diurnal factors, increasing in the lifetime of the diurnally driven convection offshore from WCS. We hypothesize that this influence was related to the outer limit of the convective envelope in the direction of the moist Kelvin wave propagation over the eastern IO before the Kelvin wave arrived in Sumatra, as will be discussed below.

Three eastward propagating disturbances were identified during the austral summer December-January-February (DJF) in 2015-2016 using the BT from the 10.4 μm spectral band of Himawari-8 AHI (Fig. 3). The large-scale mechanisms were identified based on the WH04 index, the analysis of meteorological variables, and wavenumber-frequency filtered OLR. Two of the eastward propagating cloud systems present in early December 2015 and February 2016 correspond to the convective envelope of the MJO (phases 4 and 5) moving across the MC (Fig. 3a) with easterly 850-hPa background zonal flow averaged over 6°S-6°N, which was calculated from ERA5 reanalysis (not shown). Figure 3b shows a third system propagating across the MC in January 2016 likely corresponding to a Kelvin wave disturbance propagating as bands of cloudiness in two parallel ray paths but without the characteristic westerly wind anomalies that would otherwise indicate an MJO disturbance. The ERA5 vertically integrated moisture flux convergence (VIMFC) from the

surface to the top of the atmosphere (100 hPa) was calculated to identify the convergence zone over the IO (first column in Fig. 4a,d,g,j). The positive values of VIMFC (m s^{-1})(g kg^{-1}) showed an eastward propagation towards the Maritime Continent during the squall line event. These results are consistent with the filtered OLR anomaly patterns (W m^{-2}) (second column in Fig. 4b,e,h,k), which illustrate the propagation of the Kelvin Wave. The daily accumulated satellite-derived rainfall (mm hr^{-1}) from IMERG data collection also showed comparable structures over the IO (third column in Fig. 4c,f,i,l). The rainfall signature of the Kelvin wave is observed between 11 January 2016 to 17 January 2016 with eastward propagation over the eastern IO and Sumatra, Longitude 80°E 102°E (Fig. S1 in the online supplement). The diurnally forced convection in Sumatra shows a westward propagation from the WCS, which is consistent with the brightness temperature (10.4 μm spectral band) from Himawari-8 AHI in Fig. 3b.

On 10 January 2016, the squall line was initiated by the diurnally forced convection over the land, with a subsequent extensive deep convective cloud band ~1000 km offshore from Sumatra and a lifetime (~1.5-days) that exceeds the mean lifetime of a typical structure of the diurnally driven convection in Sumatra. However, the development of the convective cells over the WCS was not uniform because differences were detected in the distribution of clouds over the North and South of Sumatra. A weak signature of a moist Kelvin wave pattern on 10 January 2016 (Fig. 4a,b,c) was identified over the southwest region of Sumatra prior to the squall line event, and the analysis confirmed the propagation of the moist Kelvin wave between Latitude 8°S and the equator (not shown); A cyclonic pattern was also observed in the wind field (Fig. 2a, b). Therefore, the residual of this first Kelvin wave might have played a role in changing the features of propagation of the squall line off the Southwest Coast of Sumatra. The dry phase of a second Kelvin wave was located over the IO on 11 January 2016 (Fig. 4d,e,f). This regional condition is not indicative of

convective coupling between the moist Kelvin wave phase and the diurnally driven convection over Sumatra for the case study period.

The dissipating stage of the squall line on 11-12 January 2016 (Fig. 4g,h,i) coincides with the edge of the convergence zone associated with the Kelvin Wave located at longitude 90°E, likely promoting the development of new convection cells. The influence of the Kelvin wave on the dissipation stage of the diurnal cycle may invigorate convection over the eastern IO. However, cold cloud cores over the eastern IO and western Maritime Continent could lead to the generation of convectively coupled Kelvin waves, as demonstrated by Roundy (2008); Kiladis et al. (2009); Baranowski et al. (2016). The Kelvin wave arrived to the WCS on 13 January 2016 (Fig. 4j,k,l). Note that the position of the Kelvin wave over the IO may play a key role in shaping the patterns of background wind and moisture distribution, changing diurnally forced convection features such as the cloud structure and propagation of the cloud population on a local scale between South and North Sumatra.

b. Diurnal Cycle and Cloud Properties

The Hovmöller diagram of filtered CTT shows the development of the squall line with a lifetime of about 1.5-days along a section perpendicular to the Northwest coast of Sumatra (Fig. 5a, green line in Figure 1). The filtered cold cloud top in Fig. 5a illustrates convective development associated with the cloud population propagating over Sumatra and the IO between 17:00 LST 10 January and 01:00 LST 12 January 2016; inland < 100 km from the WCS and over the IO ~900 km offshore. However, the lifetime of approximately 30 hours and the nominal distance of ~1000 km from the coast suggest a possible influence of non-diurnal processes and the convective invigoration near 900 km offshore. Note that the CTT increases between 200 km and 400 km offshore after 07:00 LST 11 January 2016 due to a change of propagation direction of the squall line likely associated with the

deviations of background wind induced by the easterly flow around the Sumatra mountain range. In contrast, the section perpendicular to the Southwest of Sumatra exhibits significant differences in the lifetime and the main direction of squall-line propagation, likely due to the effects of local forcings and weather conditions resulting from tropical disturbances traveling over the IO and the MC. Given the distinct responses and influences from the IO variability, the cloud evolution in the southern and northern regions of Sumatra are examined separately.

Southern Sumatra

The rapid development of the westward-propagating squall line results from local and regional forcings such as background wind flow, topography, the orientation of the east and the west coast of southern Sumatra, and tropical convection from the IO. The cloud population located onshore during the days 10-12 January 2016 is explained by the convective initiation and the westward propagation regime over the western and eastern coasts of Sumatra (Fig. 5b, red line in Figure 1). For example, on 13 January 2016, both eastward and westward propagation was identified at the West and East coast of Sumatra. The evolution of these MCSs develops a convergence line over the South-central portion inland resulting in a wide area of deep convective clouds. The diurnally driven convection signature over the WCS is identified between 17:00 LST 10 January 2016 and 07:00 LST 11 January 2016 (Fig. 5b) with a horizontal extension of ~200 km off Sumatra, starting the propagation near the coastline (0 km). A fast transition to deep convective clouds is identified within the first 200 km off Sumatra. The mean value of the CTT of the deepest cloud tops is 210 K with CTH ranging from 9 to 14 km, whereas the production of the shallow clouds dominates the convection over the IO with fast convective transitions and a CTT of roughly 240 K. This is the result of two DCs developing simultaneously over the east and WCS. The well-defined structure of cloudiness linked with a cyclonic circulation offshore South Sumatra on 09 January 2016 drives

the regional condition that inhibits the development of the convection cells over IO on 10 January 2016.

Northern Sumatra

The developments of retrieved CTH and CTT as a function of distance from the northern coastline are presented in Fig. 6. Within the first 200 km from the coast, a maximum deep open-sea convection is identified by maximum values of the CTH between 12 km and 15 km (thin grey line) (Fig. 6a) and a CTT range of 204-220 K (Fig. 6b). The transition is observed at 200-300 km from the West Coast, where the CTHs drop to ~12 km and the CTTs rises to 220 K. The second maximum of the CTH is detected offshore from Sumatra at 350-500 km, where the top of the convective system rises to 14 km. Here the CTH is shallower compared to the previous CTH close to the WCS. It is noted that the 90^{th} percentile of CTH and the minimum CTTs correspond strongly with the envelope of the convection (Fig. 6a), suggesting strong convection and areas of overshooting cloud tops and providing evidence of the location of the updrafts during the squall-line propagation. From 900 km outwards, the CTT (Fig. 6b) and the CTH values rise quickly again (Fig. 6a), likely suggesting a new convective initiation located ahead of the outflows of the dissipating squall line. We hypothesize that this resulted from the feedback between the dissipating stage of cloud population of the diurnally forced convection and the line of convergence associated with the convective envelope of the moist Kelvin wave over the eastern IO moving towards the MC.

Differential propagation of the convective envelope from north and south of Sumatra

The squall line propagation offshore from Sumatra was explored by analyzing the cold cloud cores, convective cloud mask, and cell tracking algorithm, allowing for the analysis of the spatial distribution, lifetime, and propagation speed of the cloud population. Figure 7 presents an analysis of cold cloud cores to provide evidence of multiple convection cores inside of convective envelope of the squall line propagating offshore Sumatra. Cold convective cores are presented every 3

hours, starting from panel (a) to (l), and show the cloud structure consisting of multiple types of cells, propagating as envelopes of convection offshore Sumatra. The number of cells indicates a maximum of cold cloud cores between midnight and early in the morning in Fig. 7m, and a second peak is also observed around 16:00 LST on 11 January 2016, when the signature of the diurnally driven convection merges with preexistent convection over the eastern IO (the northern hemisphere region). The nighttime convection over the IO around midnight on 12 January 2016 may indicate the first effect of the approaching Kelvin Wave (Please see the location of the Kelvin Wave in Fig. 4h and the VIMFC in Fig 4g). Figure 8 shows an example of the convective cloud mask (2 km spatial- and 10 minutes temporal-resolution) at 14:20 LST 11 January 2016 overlaid by the trajectories of the convective cells over 30 hours as the squall line propagates offshore from Sumatra (Latitude 0°/Longitude 92°E).

The cloud type categorization shows the spatial variability of the overshooting cells organized into the mesoscale structure when the cloud system moves offshore from Sumatra, suggesting possible positions and strength of updrafts at the different convective stages of the squall line. While the overshooting regions may be inferred from the Himawari-8 AHI derived cloud tops, an overpass of the CloudSat satellite during the squall line event detects the cloud vertical structure at 14:25 LST 11 January 2016 (black dots in Fig. 8). In Fig. 9, the vertical cross-section of reflectivity corresponds to the mature stage of the squall line about 400 km in the open sea (Fig. 6a and 6b). The average CTH of ~13 km and the CTT of ~204 K are comparable with those derived from Himawari-8 AHI (Fig. 5). The reflectivity captured the active section of the squall system, whose structure is somewhat analogous to a canonical leading-line/trailing-stratiform MCS (e.g., Houze 2018). An overshooting top was apparent at the leading edge of the storm (around 1°N), where the strongest updraft was likely located. Intense precipitation was generated within the cumulonimbus, with with a region of more intense precipitation present at the outer edge of the

updraft/downdraft side of the storm (1°-2.5°N), as evidenced by the strong attenuation of the radar reflectivity below the cloud base. Early studies (Houze 2004; Cotton et al. 2011) have suggested that, in the mature stage of squall lines, moistening above the boundary layer (3-5) km and moisture in the environment are critical to forming a deep, precipitating stratiform-anvil cloud. The cloud layer present at 3-8 km (1°-2.5°N) provides evidence of atmosphere moistening in the troposphere, which is indicative of the cycle of maintenance of convection during the propagation of the squall line.

The development of deep convective clouds and the inferred lifetime of the squall line for North Sumatra is presented in Fig. 10a. The deep convective cloud center is identified during the tracking using the deep convective cloud category from the convective mask and the BT channel 13 (10.4 μm spectral band). The target area is defined by the spatial distribution of each category from the convective mask every 10-minutes, along the red dots in Fig. 8, which represents the center of the cloud system associated with squall-line propagation. In Fig. 10a, three categories are presented: immature (IM) in blue, mature (M) in green, and deep convection (M_DC) in yellow. Together, these categories show the temporal development of the squall line. An increased number of pixels is observed for M and M_DC during 16 h and 28 h after the convective initiation. This provides evidence of a population of deep convective clouds propagating offshore as the squall line develops towards its mature stage. After the change in the propagation direction offshore, the trend reverses, indicating the dissipating stage of the squall line. However, rather than continuing to dissipate, a new convection cell immediately develops (green line after 01:00 LST 12 January 2016), and an increase of IM pixels is observed over the IO, showing the oceanic influence on the diurnally forced convection analyzed (~30 hours).

The southwest of Sumatra is characterized by two westward propagating systems originating from land in southeastern Sumatra and the WSC. The track suggests a deflection of the main direction

of propagation towards the northwest, moving parallel to the long axis of the island, from southern to central Sumatra (see purple dots in Fig. 8), resulting in changes in the structure and cloud distribution of the squall line. Notable features include (Fig. 10b): (1) convective initiation occurs at approximately 13:00 LST 10 January 2016, representing 5 hours of delay in time in comparison to the North section, as suggested by the convective mask and backward trajectory. Deep and cold cloud tops dominate the early stage of the convection; the structure of the convective cells is well defined over the land and along to the WCS (see the CTT at 19:00 LST 10 January 2016 near the WCS in Fig. 5b), which is confined into small areas with intense cloud activity, (2) the propagation of deep convective cells started ~5 hours before the North, and (3) the lifetime is observed to be ~11 hours, but the maximum number of M and M_DC pixels are detected between 20:00 LST 10 January 2016 and 07:00 LST 11 January 2016 (Fig. 10b), and differences in the propagation speed between land and ocean are observed. The cell-size identified as a deep convective cloud is observed to be considerably smaller than that in the northwest.

The horizontal velocity of the squall line was estimated, assuming the WCS as a reference. The best fit method based on the least-squares regression (Wilks 2011) was used to estimate the trend line after the cloud system was tracked by projecting the consecutive storm positions to a section perpendicular to the coastline, starting from northwestern Sumatra to the eastern IO. In addition, verification was performed (not shown) to ensure that there were no significant jumps in the tracked positions. Before the propagation started at 19:00 LST 10 January 2016 (Fig. 11a), at 0 km, convective initiation was located near the mountains, and the convection cell moves parallel to the coastline for 4 hours (dots without perpendicular displacement). Two main perpendicular propagation speeds are found (Fig. 11a); The first component is located between 0 and 300 km offshore with a propagation speed of ~5 m s^{-1}; standard deviation of 2.1 m s^{-1} and coefficient of determination of 95%, while a change in the propagation speed occurs at around 13:00 LST 11

January 2016 in the region 250-650 km offshore, estimated to be 10 m s^{-1}; standard deviation 1.8 m s^{-1}, and coefficient of determination of 96% is consistent with an IGW. At 650 km, the propagation of the cloud system ceased, while new convection cells were triggered near the outflow anvil when the squall line was at its dissipating stage.

The range of speeds estimated in the South of Sumatra corresponds to a double westward propagation originating from the East and West sides of Sumatra, which are based on convection cell identification during the squall line event. Even though the disturbances have the same direction of propagation, two different speeds are extracted from the analysis. Figure 11b shows the inferred speed originating from the East coast at ~7 m s^{-1} (yellow dots); standard deviation of 1.6 m s^{-1} and coefficient of determination of 98%, while the red dots indicates the convection cells off the Southwest coast of Sumatra with a speed of approximately 5 m s^{-1}; standard deviation of 1.7 m s^{-1} and coefficient of determination of 90%, which is comparable to the speed calculated near the coast at North of Sumatra (See the first speed in Fig. 11a). The westward propagation is influenced both by the interconnection between the East and the WCS and the reduction in propagation distance from the WCS, due to the large-scale disturbances traveling toward the MC over the IO. The asymmetry of background wind flow on either side of the equator may explain the differences in propagation distance between North and South Sumatra. The cyclonic circulation between the equator and 10°S that extends over most of the IO and from lower- and mid-levels (Fig. 2a,b) changed the direction of background wind flow off Sumatra limiting the propagation offshore of the squall line near southwest Sumatra. The convergence center near Sumatra is related to the interaction of the IO flow with the mountain range of the Malay Peninsula and southwest Sumatra. However, the convergence center is extended over the IO with the counterclockwise turning winds that cross the equator. Coincident with the convergence center over the eastern IO and South

Sumatra is a maximum in 925-850 hPa relative vorticity in Fig. 2c. In contrast, a zonal component of the background wind at 700 hPa in Fig. 2b is observed at the North of Sumatra and over the IO.

4. Discussion

We have investigated a squall line event off the WCS using the atmospheric and cloud products derived from the Himawari-8 satellite. The broad characteristics of the case examined are generally consistent with previous studies where observational and atmospheric numerical models were employed (e.g., Mori et al. 2004; Short et al. 2019; Yokoi et al. 2017; Bai et al. 2021). However, the high temporal, spatial, and spectral resolutions of Himawari-8 AHI have allowed us to examine the influences of the development, and internal structure of the MCS propagating offshore from Sumatra in unprecedented detail, which, to the authors knowledge, is the first investigation of its kind.

During the analyzed squall line event, the evolution of the diurnally driven convection in Sumatra is influenced by background wind (easterly) and the propagation of the moist Kelvin wave phase over the IO towards the MC (Fig. 3). This result suggests that the cloudiness propagating eastward in January 2016 in Fig. 3 responds to the globally propagating Kelvin wave. The dry Kelvin wave drives the local conditions promoting the suppressed convective phase over Sumatra, resulting in more clear sky conditions that favor local evaporation over the Indo-Pacific warm pool (IPWP) surrounding Sumatra (SST $\geq$ 28.5°C). The weekly SST anomaly over the IPWP between 10-16 January 2016 was positive ~1 K (not shown). The Kelvin wave and MJO activity are considered as the primary mechanisms that may modify the MCS lifetime and horizontal extension over the open sea (Kiladis et al. 2009; Baranowski et al. 2016; Chen et al. 2019). The redistribution of water vapor into the atmospheric column and temperature variations near the tropical troposphere has been considered as a driver of the moisture content that promotes enhanced convection during

the propagation of Kelvin waves (Tsuda et al. 1994a,b; Shimizu and Tsuda 1997). However, in the case studied here, the squall line (Fig. 3; zonal section) is located close to the edge of the area influenced by the moist Kelvin wave, and the brightness temperature from the water vapor channels of Himawari-8 AHI provided evidence that moisture is transported in the lower-middle (Animation A in the online supplement) troposphere, upper troposphere (Animation B in the online supplement), and a Hovmöller diagram of total column water vapor anomaly from ERA to provide evidence of source of moisture over the eastern IO (Fig. S2 in the online supplement).

Two responses in the offshore propagation of the cloud population are found for the Northwest and South of Sumatra: Over the Northwest of Sumatra, the westward propagation of the cloud system shows a lifetime of ~1.5-days and an offshore propagation distance of approximately 1000 km from Sumatra. The first stage of the squall line propagation, which is associated with the regular diurnal activity of rainfall and cloudiness in Sumatra, has two propagation speeds: 5 m s^{-1} within 0-300 km and 12 m s^{-1} over the open sea. In the second part, the cloud population between 800-1000 km offshore is associated with the convection over the IO and the Western part of the Indio-Pacific MC, coinciding with the Kelvin wave activity in January 2016. Besides, the CTT of the deep convective cells was recorded to be ~220 K. However, at 800 km, new convective cells emerged, likely due to the instability associated with a cyclonic circulation located over the eastern IO with an eastward propagation. In contrast, over southern Sumatra, the deepest convection is located onshore. Two different speeds characterize the westward propagation originating from the East and West coasts: 7 m s^{-1} and 5 m s^{-1} respectively. The propagation offshore was limited to within the first 200 km, most likely by the dry phase of the Kelvin wave activity over the IO (Fig. 3b); after that, the cloud population deflected to the Northwest due to convective activity associated with a cyclonic circulation over the eastern IO. This modified the wind flow over the IO near the WCS, changing the trajectory and lifetime of the squall line.

The westward propagation of the squall line between 5°N and 5°S and the ~1.5-day lifetime of the cloud system corresponding to IGWs with westward propagation under the MJO break period partially agrees with previous studies where information from older geostationary satellites was used, although the exact mechanisms involved in driving the prolonged life cycle are still under debate. From TOGA COARE and MISMO, Takayabu et al. (1996), Chen and Houze (1997), and Yamada et al. (2010) suggested that the 2-days periodicity results from the nonlinear interaction between stratiform clouds, radiation, and surface processes, and the importance of the lower- and-upper-levels coupling among convection to the 2–3 days occurrence of convection. Recent studies demonstrate that the mesoscale process and the role of stratiform are critical to the quasi-2-day lifetime, which closely corresponds to the convectively active regions under large-scale forcings (Yu et al. 2018, 2021). In our case study, a westward propagation of cloudiness is observed between central and northwestern Sumatra during the afternoon (Fig. 5a). While both local and external factors might generate convective initiation, there is likely a two-way feedback between the background convection over the IO, the local circulations, and flow direction. The convective initiation and direction of propagation of the squall line along the northern coast of Sumatra were influenced by of the convective activity over the IO during the dissipating stage of the squall line. First, the propagation follows the mountain range orientation, after which, the cloud population modified the direction moving towards the open sea (see red dots over Sumatra Fig. 8). Despite that, the ~2-day frequency of convection is usually found in convectively favorable larger-scale conditions. In this case study, the mesoscale process and the local condition may be more significant to the development of the squall line, and the prolonged lifetime of the convective event could be linked to the arriving Kelvin wave during the dissipation stage of the squall line over the IO.

The high-resolution Himawari-8 AHI satellite data allows us to identify the position of the deep convective cells associated with strong topographic influence in the North of Sumatra (Fig. 12).

The deep convection was located over the coastline close to the mountain ridge. Meanwhile, in the section located a few kilometers south (see the blue line in Fig. 1), the cloud system was identified inland within the first 100 km from the WCS (Fig. 12b). The Hovmöller diagrams of BT 10.4 μm show that the convection occurred in the afternoon, which was likely forced by radiative heating, sea- and mountain-breeze systems, and associated with moisture convergence. Indeed, previous studies have proposed that convective initiation during the afternoon is associated with convergence occurring over the mountains and diabatic heating anomalies (e.g., Qian 2008; Peatman et al. 2014; Hassim et al. 2016; Vincent and Lane 2016). This agrees with the evolution of the diurnally driven convection and the role of the mountains over Colombia in destabilizing parcels close to the surface to trigger convection during the late afternoon (Mapes et al. 2003). The retrieved CTT showed a cold and deep region of clouds of ~206 K in the vicinity of the mountains, propagating westward off Sumatra, which corresponds with the main direction of displacement of the cloud system. Over the mountains with lower cloud tops, the CTT was ~222 K, and the propagation of the cloud population shifted eastward onshore. Cloudiness from Himawari-8 AHI propagation of deep convective cells in opposite directions starting from the top of the mountains (Fig. 12), which is consistent with the linear theory of the tropical land- sea-breeze (Rotunno 1983; Weisman and Rotunno 2004; Qian et al. 2012, 2009). Our results show some similarities with the case of two waves propagating in opposite directions and asymmetric response offshore/onshore due to the influence of the background wind flow. Secondary structures with eastward propagation associated with the main cloud system are observed when the squall line is positioned over the IO (Fig. 5a). These small structures emerge, indicating unsettled conditions in the outflow region behind the leading line.

The internal structure of the squall line propagation was analyzed by the temporal development of the multiple cold cloud cores (Fig. 7). Employing M (late peak) and M_DC (early peak)

categories of the convective mask (Fig. 10). The number of pixels initially increases in both categories and the CTT decreases as a function of time (not shown). The maximum number of pixels of M_DC was reached at 07:00 LST 11 January 2016. After that, the proportion of the number of pixels of the two categories was inverted, and the M class area increased rapidly in the late stage of the squall line at 16:00 LST 11 January 2016. The infrared radiation-based analysis identifies the large areas of the anvil cloud, which is useful in studying MCS areal coverage, but not necessarily helpful in discriminating the internal vertical structure of cloud system such as updrafts, and there is insufficient information in infrared radiation imagery to infer the dynamical and in-cloud microphysical processes associated with the convective and stratiform contributions of rainfall. However, we have divided between deep convection regions that include the anvil region and the intense region with overshooting cloud tops, allowing us to identify the convective trends within the cloud system during the propagation.

The propagation may be explained as the modulation of the diurnally driven convection by IGWs initiated by diurnally oscillating heating and cooling over the land with a propagation speed of $\sim$12 m s^{-1} with an enhancement in mature clouds approximately at 13:00 LST 11 January 2016 (Fig. 10a), as a result of the transition from density current dominated to IGW dominated at 240 km. However, the southern section maintained a slower propagation speed more consistent with density currents $\sim$5 m s^{-1}. The tropical disturbances located over the IO controlled the convection at a local scale near the southwestern coast. First, the DC processes are driven by wave-induced convergence, the influence of the vertical distribution of moisture, and the static stability in the atmosphere column, particularly in the middle- and upper-troposphere (Mapes et al. 2003; Lane and Reeder 2001; Tulich and Mapes 2008; Vincent and Lane 2016). Secondly, the large-scale environment controls the distance of the cloud population over the open sea under the westward propagation regime. Takayabu (1994); Roundy (2008); Rauniyar and Walsh (2011); Vincent

and Lane (2016); Ruppert and Zhang (2019); Sakaeda et al. (2020); Seiki et al. (2021b) have explored the effects of large-scale forcing on the diurnal cycle of rainfall and cloudiness in the Tropics, during enhanced, suppressed convection of the MJO or the activity of equatorial waves. Thirdly, the influence ahead of the convective envelope of the approaching Kelvin wave initiates an apparent extension of the squall line. Here our case study is an example of how the diurnally driven convection develops despite the suppressed MJO phase and the Kelvin wave propagating over the eastern IO. The meridional response is associated with the interplay of various weather regimes over the WCS and the IO, as well as of the geometry and topography of Sumatra. Among other things the differences between the North and South squall line propagation speeds suggest complexity in the role of the IGWs, which would have been lost without this detailed analysis.

5. Conclusions

Using a range of satellite-based and reanalysis datasets including the unprecedented high-resolution Himawari-8 AHI products, this study presents a detailed investigation of the evolution of a Sumatra squall line event in space and time. Key aspects of the investigation include:

- characterizing the squall line system by linking the retrieved cloud properties, surface precipitation and dynamical processes across a range of spatiotemporal scales;
- detailing the continuous propagation of the squall line by tracking the convection cells during the lifetime of the diurnally driven convection over Sumatra;
- presenting evidence of two distinct responses of the diurnally forced convection over Sumatra and how they evolve under different local and large-scale forcings (including the influence of the approaching Kelvin wave during the dissipation stage of the event);
- identifying multiple types of convection cells within the squall line cloud system, whose propagation are not uniform;

- demonstrating the capability to continuously track deep convective activities over the Sumatra with high-resolution Himawari-8 observations, which adds a new dimension to studying the MCSs in this region.

Our analysis demonstrates that offshore propagation of tropical squall lines is by no means a single or simple physical phenomenon. A number of inter-related mechanisms are involved in the overall sea-ward propagation of the diurnally initiated convection over Sumatra. In the North of Sumatra, these include: Near-shore propagation related to density currents, far-offshore propagation related to internal gravity waves, and the lifetime extension of the squall line when the diurnally driven convection approaches the edge of the convective envelope of the Kelvin wave over the eastern IO. In the South of Sumatra, these include: Distinct westward propagating squall lines from the east and west coasts of Sumatra modulated by the flow pattern around the southern Sumatra mountain range, offshore propagation related to density currents, background winds changes, and short lifetime of the squall line due to local weather context including the weak signature of the prior Kelvin wave ahead of the squall line event.

The state-of-the-art datasets allowed a detailed view of the evolution of a mesoscale convective system and its variation along Sumatra and the Indian Ocean The derived satellite products tracked the development of the westward propagation of the cloud system off the northwest coast of Sumatra with a distance of ~1000 km offshore and a lifetime ~30 h. In contrast, analysis of the propagation over the southwest coast of Sumatra indicated that convection over the Indian Ocean modified the squall line structure. The convective initiation associated with the land-, sea-breeze systems had a time lag of approximately 5 hours between North and South of Sumatra. However, the observed diurnal cycle and the latitudinal responses are modified by Kelvin wave activity at the regional scale. This showed that there is 2-way feedback between mesoscale processes over Sumatra and

the convection over the IO, which adds complexity to the evolution of the offshore propagating squall line.

Retrieved cloud properties and tracking of the offshore propagation indicated the cloud structure consists of multiple types of convection cells, whose propagation is not uniform. Thus the mean propagation signatures that have been previously reported to be perpendicular to the coastline are better defined as envelopes of convection rather than squall lines themselves. The internal variability of the cloud population was identified in two regions at 100 km and 400 km off Sumatra with cloud top height in the 90^{th} percentile, reaching cloud top temperatures of ~204 K. A cross-section of cloud radar reflectivity from the CloudSat satellite revealed the cloud vertical structure of the squall line at its mature stage consistent with a canonical leading-line / trailing-stratiform system, generally in agreement with the inferred characteristics from Himawari-8 AHI data. The maximum area of the convective mask was associated with the transition between convective regimes during the propagation of the squall line. The internal structure and lifetime of the squall line were analyzed by using the convective mask and cell-tracking algorithm to identify the early peak of deep convective cells (the coldest clouds) and late peak associated with cloud classified as mature, showing the signature of the tropical MCS.

In studying a single case of offshore propagation at high-resolution, the offshore MCSs propagation in the tropics is shown to be a composite process, including density currents, gravity waves, background wind flow regimes, and moisture. The propagation of the squall line indicated two different speeds: (1) The first component was located at 0-300 km off Sumatra with a speed of ~5 m s^{-1} similar to typical density current speeds, and (2) the far-offshore cloudiness moved at a mean propagation speed of 12 m s^{-1} over the eastern Indian Ocean. Indicating the afternoon convection has been suggested to be forced by radiative heating, sea- and mountain-breeze systems, moisture transport, and topographically forced flows, and inertia–gravity wave propagation initiated by di-

urnally oscillating heating and cooling over the land, as proposed in a number of previous studies (e.g., Vincent and Lane 2016; Mapes et al. 2003; Lane and Reeder 2001; Tulich and Mapes 2008; Ruppert and Zhang 2019). However, the coupling to an IGW was only clear for the northern line, and the southern line only showed a the slower speed of propagation of the diurnally driven convection. This highlighted the complexity of the gravity wave convection coupling for the offshore propagating convection, which warrants further investigation in future studies. At the dissipating stage of the squall line, the contribution of the IO promotes the initialization of new convective cells, which interact with the Kelvin wave activity and the warm pool of ocean water at the Western of the Indio-Pacific MC in January 2016.

This study has explored the development of a single squall line event over the western seas of Sumatra with the analysis of the effects between the diurnally driven convection over Sumatra and the source of tropical variability at the local scale using the high spatiotemporal and spectral resolution data from Himawari-8 AHI and CSPP-Geo Geocat. The unprecedented level of detail that can be uncovered by this high-resolution satellite dataset has proven valuable in understanding the development of MCSs over the MC, and potentially other regions within the field of view of the satellite. This work has implications for understanding future weather and climate extremes in the region and set the stage for statistical analysis of longer datasets. Further work is necessary to expand the results into the austral summer DJF for multiple years, using the historical data of Himawari-8 AHI, and to study the dynamics of land-sea- valley-mountain-breeze systems and gravity wave propagation with the incorporation of convective permitting simulations.

Acknowledgments. This work was funded by the Melbourne Research Scholarship and the Australian Research Council's (ARC) Discovery Project DP190100786 for C. Lopez-Bravo and the ARC Centre of Excellence for Climate Extremes CE170100023 for C. Vincent, Y. Huang, and

T. Lane. The production of derived-satellite data from Himawari-8 AHI for this research was undertaken on the NCI National Facility in Canberra, Australia, supported by the Australian Commonwealth Government. The authors wish to thank the three reviewers for their insightful feedback. The JMA Meteorological Satellite Center, The Bureau of Meteorology, Australia, and the CSPP-Geo project (CIMSS - UW-Madison). Thanks also to Paola Petrelli of the University of Tasmania and Kelsey Druken of the Australian National University for all the facilities during the dataset publication process, and Scott Wales of the University of Melbourne for technical support.

References

Albright, M. D., D. R. Mock, E. E. Recker, and R. J. Reed, 1981: A Diagnostic Study of the Diurnal Rainfall Variation in the GATE B-Scale Area. *J. Atmos. Sci.*, **38 (7)**, 1429–1445, doi: 10.1175/1520-0469(1981)038<1429:ADSOTD>2.0.CO;2.

Bai, H., and Coauthors, 2021: Formation of Nocturnal Offshore Rainfall near the West Coast of Sumatra: Land Breeze or Gravity Wave? *Mon. Wea. Rev.*, **149 (3)**, 715 – 731, doi:10.1175/MWR-D-20-0179.1.

Banzon, V., T. M. Smith, T. M. Chin, C. Liu, and W. Hankins, 2016: A long-term record of blended satellite and in situ sea-surface temperature for climate monitoring, modeling and environmental studies. *Earth Syst. Sci. Data*, **8 (1)**, 165–176, doi:10.5194/essd-8-165-2016.

Baranowski, D. B., M. K. Flatau, P. J. Flatau, and A. J. Matthews, 2016: Phase locking between atmospheric convectively coupled equatorial Kelvin waves and the diurnal cycle of precipitation over the Maritime Continent. *Geophys. Res. Lett.*, **43 (15)**, 8269–8276, doi: 10.1002/2016GL069602.

Birch, C. E., S. Webster, S. C. Peatman, D. J. Parker, A. J. Matthews, Y. Li, and M. E. E. Hassim, 2016: Scale Interactions between the MJO and the Western Maritime Continent. *J. Climate*, **29 (7)**, 2471 – 2492, doi:10.1175/JCLI-D-15-0557.1.

Chen, S. S., and J. Houze, Robert A., 1997: Diurnal variation and life-cycle of deep convective systems over the tropical pacific warm pool. *Quart. J. Roy. Meteor. Soc.*, **123 (538)**, 357–388, doi:10.1002/qj.49712353806.

Chen, S. S., J. Houze, Robert A., and B. E. Mapes, 1996: Multiscale Variability of Deep Convection In Realation to Large-Scale Circulation in TOGA COARE. *J. Atmos. Sci.*, **53 (10)**, 1380–1409, doi:10.1175/1520-0469(1996)053<1380:MVODCI>2.0.CO;2.

Chen, W.-T., S.-P. Hsu, Y.-H. Tsai, and C.-H. Sui, 2019: The Influences of Convectively Coupled Kelvin Waves on Multiscale Rainfall Variability over the South China Sea and Maritime Continent in December 2016. *J. Climate*, **32 (20)**, 6977–6993, doi:10.1175/JCLI-D-18-0471.1.

Cotton, W. R., G. Bryan, and S. C. van den Heever, 2011: Chapter 9 - Mesoscale Convective Systems. *Storm and Cloud Dynamics*, W. Cotton, G. Bryan, and S. van den Heever, Eds., International Geophysics, Vol. 99, Academic Press, 455–526, doi:10.1016/S0074-6142(10)09915-8.

Feng, Z., L. R. Leung, R. A. Houze Jr., S. Hagos, J. Hardin, Q. Yang, B. Han, and J. Fan, 2018: Structure and Evolution of Mesoscale Convective Systems: Sensitivity to Cloud Microphysics in Convection-Permitting Simulations Over the United States. *J. Adv. Model. Earth Syst.*, **10 (7)**, 1470–1494, doi:https://doi.org/10.1029/2018MS001305.

Fetterer, F., J. Stewart, and W. Meier, 2015: Updated daily. MASAM2: Daily 4 km Arctic Sea Ice Concentration, Version 1, indicate subset used, Boulder, Colorado USA, NSIDC: National

Snow and Ice Data Center. doi:10.7265/N5ZS2TFT.

Fine, C. M., R. H. Johnson, P. E. Ciesielski, and R. K. Taft, 2016: The Role of Topographically Induced Vortices in Tropical Cyclone Formation over the Indian Ocean. *Mon. Wea. Rev.*, **144 (12)**, 4827 – 4847, doi:10.1175/MWR-D-16-0102.1.

Fujita, M., K. Yoneyama, S. Mori, T. Nasuno, and M. Satoh, 2011: Diurnal Convection Peaks over the Eastern Indian Ocean off Sumatra during Different MJO Phases. *J. Meteor. Soc. Japan*, **89A**, 317–330, doi:10.2151/jmsj.2011-A22.

Hassim, M. E. E., and T. P. Lane, 2010: A model study on the influence of overshooting convection on TTL water vapour. *Atmos. Chem. Phys.*, **10 (20)**, 9833–9849, doi:10.5194/acp-10-9833-2010.

Hassim, M. E. E., T. P. Lane, and W. W. Grabowski, 2016: The diurnal cycle of rainfall over New Guinea in convection-permitting WRF simulations. *Atmos. Chem. Phys.*, **16 (1)**, 161–175, doi:10.5194/acp-16-161-2016.

Houze, R. A., 2004: Mesoscale convective systems. *Rev. Geophys.*, **42 (4)**, doi:10.1029/2004RG000150.

Houze, R. A., 2018: 100 Years of Research on Mesoscale Convective. *Meteor. Mon.*, **59**, 17.1 – 17.54, doi:10.1175/AMSMONOGRAPHS-D-18-0001.1.

Houze, R. A., S. G. Geotis, F. D. Marks, and A. K. West, 1981: Winter Monsoon Convection in the Vicinity of North Borneo. Part I: Structure and Time Variation of the Clouds and Precipitation. *Mon. Wea. Rev.*, **109 (8)**, 1595 – 1614, doi:10.1175/1520-0493(1981)109<1595:WMCITV>2.0.CO;2.

Huang, Y., S. Siems, M. Manton, A. Protat, L. Majewski, and H. Nguyen, 2019: Evaluating Himawari-8 Cloud Products Using Shipborne and CALIPSO Observations: Cloud-Top Height

and Cloud-Top Temperature. *J. Atmos. Oceanic Technol.*, **36 (12)**, 2327–2347, doi:10.1175/JTECH-D-18-0231.1.

Huffman, G. J., D. T. Bolvin, E. J. Nelkin, and J. Tan, 2015: Integrated Multi-satellitE Retrievals for GPM (IMERG) technical documentation. *NASA/GSFC Code*, **612 (47)**, 2019.

Johnson, J. T., P. L. MacKeen, A. Witt, E. D. W. Mitchell, G. J. Stumpf, M. D. Eilts, and K. W. Thomas, 1998: The storm cell identification and tracking algorithm: An enhanced wsr-88d algorithm. *Wea. Forecasting*, **13 (2)**, 263 – 276, doi:10.1175/1520-0434(1998)013<0263:TSCIAT>2.0.CO;2.

Kiladis, G. N., C. D. Thorncroft, and N. M. J. Hall, 2006: Three-Dimensional Structure and Dynamics of African Easterly Waves. Part I: Observations. *J. Atmos. Sci.*, **63 (9)**, 2212 – 2230, doi:10.1175/JAS3741.1.

Kiladis, G. N., M. C. Wheeler, P. T. Haertel, K. H. Straub, and P. E. Roundy, 2009: Convectively coupled equatorial waves. *Rev. Geophys.*, **47 (2)**, doi:10.1029/2008RG000266.

Lane, T. P., and M. J. Reeder, 2001: Convectively Generated Gravity Waves and Their Effect on the Cloud Environment. *J. Atmos. Sci.*, **58 (16)**, 2427 – 2440, doi:10.1175/1520-0469(2001)058<2427:CGGWAT>2.0.CO;2.

Liebmann, B., and C. A. Smith, 1996: Description of a Complete (Interpolated) Outgoing Longwave Radiation Dataset. *Bull. Amer. Meteor. Soc.*, **77 (6)**, 1275–1277.

Lopez-Bravo, C., C. L. Vincent, and Y. Huang, 2021a: Himawari-8 GeoCat 1.0.3 Australian Domain Level 1 v1.0. *NCI National Research Data Collection*, doi:10.25914/60096221a8f7a.

Lopez-Bravo, C., C. L. Vincent, and Y. Huang, 2021b: Himawari-8 GeoCat 1.0.3 Australian Domain Level 2 v1.0. *NCI National Research Data Collection*, doi:10.25914/60096228c7ec0.

Love, B. S., A. J. Matthews, and G. M. S. Lister, 2011: The diurnal cycle of precipitation over the Maritime Continent in a high-resolution atmospheric model. *Quart. J. Roy. Meteor. Soc.*, **137 (657)**, 934–947, doi:10.1002/qj.809.

Machado, L. A. T., J.-P. Duvel, and M. Desbois, 1993: Diurnal Variations and Modulation by Easterly Waves of the Size Distribution of Convective Cloud Clusters over West Africa and the Atlantic Ocean. *Mon. Wea. Rev.*, **121 (1)**, 37–49, doi:10.1175/1520-0493(1993)121<0037:DVAMBE>2.0.CO;2.

Maddox, R. A., 1980: Mesoscale convective complexes. *Bull. Amer. Meteor. Soc.*, 1374–1387.

Mapes, B., and R. A. Houze Jr., 1992: An Integrated View of the 1987 Australian Monsoon and Its Mesoscale Convective Systems. I: Horizontal Structure. *Quart. J. Roy. Meteor. Soc.*, **118 (507)**, 927–963, doi:10.1002/qj.49711850706.

Mapes, B., S. Tulich, J. Lin, and P. Zuidema, 2006: The mesoscale convection life cycle: Building block or prototype for large-scale tropical waves? *Dyn. Atmos. Oceans*, **42 (1)**, 3 – 29, doi:10.1016/j.dynatmoce.2006.03.003.

Mapes, B. E., T. T. Warner, and M. Xu, 2003: Diurnal Patterns of Rainfall in Northwestern South America. Part III: Diurnal Gravity Waves and Nocturnal Convection Offshore. *Mon. Wea. Rev.*, **131 (5)**, 830–844, doi:10.1175/1520-0493(2003)131<0830:DPORIN>2.0.CO;2.

McGarry, M. M., and R. J. Reed, 1978: Diurnal Variations in Convective Activity and Precipitation During Phases II and III of GATE. *Mon. Wea. Rev.*, **106 (1)**, 101–113, doi:10.1175/1520-0493(1978)106<0101:DVICAA>2.0.CO;2.

Mecikalski, J. R., and K. M. Bedka, 2006: Forecasting Convective Initiation by Monitoring the Evolution of Moving Cumulus in Daytime GOES Imagery. *Mon. Wea. Rev.*, **134 (1)**, 49–78, doi:10.1175/MWR3062.1.

Merk, D., and T. Zinner, 2013: Detection of convective initiation using Meteosat SEVIRI: implementation in and verification with the tracking and nowcasting algorithm Cb-TRAM. *Atmos. Meas. Tech.*, **6 (8)**, 1903–1918, doi:10.5194/amt-6-1903-2013.

Mori, S., and Coauthors, 2004: Diurnal Land-Sea Rainfall Peak Migration over Sumatera Island, Indonesian Maritime Continent, Observed by TRMM Satellite and Intensive Rawinsonde Soundings. *Mon. Wea. Rev.*, **132 (8)**, 2021–2039, doi:10.1175/1520-0493(2004)132<2021:DLRPMO>2.0.CO;2.

Moseley, C., P. Berg, and J. O. Haerter, 2013: Probing the precipitation life cycle by iterative rain cell tracking. *J. Geophys. Res. Atmos.*, **118 (24)**, 13,361–13,370, doi:https://doi.org/10.1002/2013JD020868.

Moseley, C., C. Hohenegger, P. Berg, and J. O. Haerter, 2016: Intensification of convective extremes driven by cloud–cloud interaction. *Nat. Geosci.*, **9 (10)**, 748–752.

National Ice Center, 2008: Updated daily. MASAM2: Daily 4 km Arctic Sea Ice Concentration, Version 1, indicate subset used, Boulder, Colorado USA, NSIDC: National Snow and Ice Data Center. doi:10.7265/N52R3PMC.

NCEP, 2007: NCEP Global Forecast System (GFS) Analyses and Forecasts. Research Data Archive at the National Center for Atmospheric Research, Computational and Information Systems Laboratory, Boulder CO, doi:10.5065/D65Q4TSG.

Peatman, S. C., A. J. Matthews, and D. P. Stevens, 2014: Propagation of the Madden-Julian Oscillation through the Maritime Continent and scale interaction with the diurnal cycle of precipitation. *Quart. J. Roy. Meteor. Soc.*, **140 (680)**, 814–825, doi:10.1002/qj.2161.

Peatman, S. C., A. J. Matthews, and D. P. Stevens, 2015: Propagation of the Madden–Julian Oscillation and scale interaction with the diurnal cycle in a high-resolution GCM. *Climate Dyn.*, **45 (9-10)**, 2901–2918.

Qian, J.-H., 2008: Why Precipitation Is Mostly Concentrated over Islands in the Maritime Continent. *J. Atmos. Sci.*, **65 (4)**, 1428–1441, doi:10.1175/2007JAS2422.1.

Qian, T., C. C. Epifanio, and F. Zhang, 2009: Linear Theory Calculations for the Sea Breeze in a Background Wind: The Equatorial Case. *J. Atmos. Sci.*, **66 (6)**, 1749 – 1763, doi:10.1175/2008JAS2851.1.

Qian, T., C. C. Epifanio, and F. Zhang, 2012: Topographic Effects on the Tropical Land and Sea Breeze. *J. Atmos. Sci.*, **69 (1)**, 130 – 149, doi:10.1175/JAS-D-11-011.1.

Rauniyar, S. P., and K. J. E. Walsh, 2011: Scale Interaction of the Diurnal Cycle of Rainfall over the Maritime Continent and Australia: Influence of the MJO. *J. Climate*, **24 (2)**, 325 – 348, doi:10.1175/2010JCLI3673.1.

Rauniyar, S. P., and K. J. E. Walsh, 2013: Influence of ENSO on the Diurnal Cycle of Rainfall over the Maritime Continent and Australia. *J. Climate*, **26 (4)**, 1304 – 1321, doi:10.1175/JCLI-D-12-00124.1.

Reynolds, R. W., T. M. Smith, C. Liu, D. B. Chelton, K. S. Casey, and M. G. Schlax, 2007: Daily High-Resolution-Blended Analyses for Sea Surface Temperature. *J. Climate*, **20 (22)**, 5473–5496, doi:10.1175/2007JCLI1824.1.

852 Roberts, R. D., and S. Rutledge, 2003: Nowcasting Storm Initiation and Growth Using GOES-8 and
853 WSR-88D Data. *Wea. Forecasting*, **18 (4)**, 562–584, doi:10.1175/1520-0434(2003)018<0562:
854 NSIAGU>2.0.CO;2.

855 Rotunno, R., 1983: On the Linear Theory of the Land and Sea Breeze. *J. Atmos. Sci.*, **40 (8)**,
856 1999–2009, doi:10.1175/1520-0469(1983)040<1999:OTLTOT>2.0.CO;2.

857 Rotunno, R., and P. K. Smolarkiewicz, 1991: Further Results on Lee Vortices in Low-Froude-
858 Number Flow. *J. Atmos. Sci.*, **48 (19)**, 2204 – 2211, doi:10.1175/1520-0469(1991)048<2204:
859 FROLVI>2.0.CO;2.

860 Roundy, P. E., 2008: Analysis of Convectively Coupled Kelvin Waves in the Indian Ocean MJO.
861 *J. Atmos. Sci.*, **65 (4)**, 1342 – 1359, doi:10.1175/2007JAS2345.1.

862 Ruppert, J., James H., and F. Zhang, 2019: Diurnal Forcing and Phase Locking of Gravity Waves
863 in the Maritime Continent. *J. Atmos. Sci.*, **76 (9)**, 2815–2835, doi:10.1175/JAS-D-19-0061.1.

864 Ruppert, J. H., X. Chen, and F. Zhang, 2020: Convectively Forced Diurnal Gravity Waves in the
865 Maritime Continent. *J. Atmos. Sci.*, **77 (3)**, 1119 – 1136, doi:10.1175/JAS-D-19-0236.1.

866 Sakaeda, N., G. Kiladis, and J. Dias, 2020: The Diurnal Cycle of Rainfall and the Convectively
867 Coupled Equatorial Waves over the Maritime Continent. *J. Climate*, **33 (8)**, 3307–3331, doi:
868 10.1175/JCLI-D-19-0043.1.

869 Sakurai, N., and Coauthors, 2009: Internal Structures of Migratory Cloud Systems with Diurnal
870 Cycle over Sumatera Island during CPEA-I Campaign. *J. Meteor. Soc. Japan*, **87 (1)**, 157–170,
871 doi:10.2151/jmsj.87.157.

Seiki, A., S. Yokoi, and M. Katsumata, 2021a: The Impact of Diurnal Precipitation over Sumatra Island, Indonesia, on Synoptic Disturbances and its Relation to the Madden-Julian Oscillation. *J. Meteor. Soc. Japan*, **advpub**, doi:10.2151/jmsj.2021-007.

Seiki, A., S. Yokoi, and M. Katsumata, 2021b: The Impact of Diurnal Precipitation over Sumatra Island, Indonesia, on Synoptic Disturbances and its Relation to the Madden-Julian Oscillation. *J. Meteor. Soc. Japan*, **99 (1)**, 113–137, doi:10.2151/jmsj.2021-007.

Serra, Y. L., X. Jiang, B. Tian, J. Amador-Astua, E. D. Maloney, and G. N. Kiladis, 2014: Tropical Intraseasonal Modes of the Atmosphere. *Annu. Rev. Environ. Resour.*, **39 (1)**, 189–215, doi:10.1146/annurev-environ-020413-134219, 10.1146/annurev-environ-020413-134219.

Shimizu, A., and T. Tsuda, 1997: Characteristics of Kelvin waves and gravity waves observed with radiosondes over Indonesia. *J. Geophys. Res. Atmos.*, **102 (D22)**, 26 159–26 171, doi:10.1029/96JD03146.

Short, E., C. L. Vincent, and T. P. Lane, 2019: Diurnal Cycle of Surface Winds in the Maritime Continent Observed through Satellite Scatterometry. *Mon. Wea. Rev.*, **147 (6)**, 2023–2044, doi:10.1175/MWR-D-18-0433.1.

Smolarkiewicz, P. K., and R. Rotunno, 1989: Low Froude Number Flow Past Three-Dimensional Obstacles. Part I: Baroclinically Generated Lee Vortices. *J. Atmos. Sci.*, **46 (8)**, 1154 – 1164, doi:10.1175/1520-0469(1989)046<1154:LFNFPT>2.0.CO;2.

Stephens, G. L., and Coauthors, 2002: THE CLOUDSAT MISSION AND THE A-TRAIN: A New Dimension of Space-Based Observations of Clouds and Precipitation. *Bull. Amer. Meteor. Soc.*, **83 (12)**, 1771–1790, doi:10.1175/BAMS-83-12-1771.

Takayabu, Y. N., 1994: Large-Scale Cloud Disturbances Associated with Equatorial Waves. *J. Meteor. Soc. Japan*, **72 (3)**, 433–449, doi:10.2151/jmsj1965.72.3_433.

Takayabu, Y. N., K.-M. Lau, and C.-H. Sui, 1996: Observation of a Quasi-2-Day Wave during TOGA COARE. *Mon. Wea. Rev.*, **124 (9)**, 1892 – 1913, doi:10.1175/1520-0493(1996)124<1892:OOAQDW>2.0.CO;2.

Takayabu, Y. N., and M. Murakami, 1991: The Structure of Super Cloud Clusters Observed in 1-20 June 1986 and their Relationship to Easterly Waves. *J. Meteor. Soc. Japan*, **69 (1)**, 105–125, doi:10.2151/jmsj1965.69.1_105.

Tsuda, T., Y. Murayama, H. Wiryosumarto, S. W. B. Harijono, and S. Kato, 1994a: Radiosonde observations of equatorial atmosphere dynamics over Indonesia: 1. Equatorial waves and diurnal tides. *J. Geophys. Res. Atmos.*, **99 (D5)**, 10 491–10 505, doi:10.1029/94JD00355.

Tsuda, T., Y. Murayama, H. Wiryosumarto, S. W. B. Harijono, and S. Kato, 1994b: Radiosonde observations of equatorial atmosphere dynamics over Indonesia: 2. Characteristics of gravity waves. *J. Geophys. Res. Atmos.*, **99 (D5)**, 10 507–10 516, doi:10.1029/94JD00354.

Tulich, S. N., and B. E. Mapes, 2008: Multiscale Convective Wave Disturbances in the Tropics: Insights from a Two-Dimensional Cloud-Resolving Model. *J. Atmos. Sci.*, **65 (1)**, 140 – 155, doi:10.1175/2007JAS2353.1.

Tulich, S. N., D. A. Randall, and B. E. Mapes, 2007: Vertical-Mode and Cloud Decomposition of Large-Scale Convectively Coupled Gravity Waves in a Two-Dimensional Cloud-Resolving Model. *J. Atmos. Sci.*, **64 (4)**, 1210 – 1229, doi:10.1175/JAS3884.1, URL https://journals.ametsoc.org/view/journals/atsc/64/4/jas3884.1.xml.

Vila, D. A., L. A. T. Machado, H. Laurent, and I. Velasco, 2008: Forecast and Tracking the Evolution of Cloud Clusters (ForTraCC) Using Satellite Infrared Imagery: Methodology and Validation. *Wea. Forecasting*, **23 (2)**, 233–245, doi:10.1175/2007WAF2006121.1.

Vincent, C. L., and T. P. Lane, 2016: Evolution of the Diurnal Precipitation Cycle with the Passage of a Madden-Julian Oscillation Event through the Maritime Continent. *Mon. Wea. Rev.*, **144 (5)**, 1983–2005, doi:10.1175/MWR-D-15-0326.1.

Vincent, C. L., and T. P. Lane, 2017: A 10-Year Austral Summer Climatology of Observed and Modeled Intraseasonal, Mesoscale, and Diurnal Variations over the Maritime Continent. *J. Climate*, **30 (10)**, 3807–3828, doi:10.1175/JCLI-D-16-0688.1.

Walker, J. R., J. MacKenzie, Wayne M., J. R. Mecikalski, and C. P. Jewett, 2012: An Enhanced Geostationary Satellite–Based Convective Initiation Algorithm for 0–2-h Nowcasting with Object Tracking. *J. Appl. Meteor. Climatol.*, **51 (11)**, 1931–1949, doi:10.1175/JAMC-D-11-0246.1.

Weisman, M. L., and R. Rotunno, 2004: "A Theory for Strong Long-Lived Squall Lines" Revisited. *J. Atmos. Sci.*, **61 (4)**, 361–382, doi:10.1175/1520-0469(2004)061<0361:ATFSLS>2.0.CO;2.

Wheeler, M., and G. N. Kiladis, 1999: Convectively Coupled Equatorial Waves: Analysis of Clouds and Temperature in the Wavenumber-Frequency Domain. *J. Atmos. Sci.*, **56 (3)**, 374–399, doi:10.1175/1520-0469(1999)056<0374:CCEWAO>2.0.CO;2.

Wheeler, M. C., and H. H. Hendon, 2004: An All-Season Real-Time Multivariate MJO Index: Development of an Index for Monitoring and Prediction. *Mon. Wea. Rev.*, **132 (8)**, 1917–1932, doi:10.1175/1520-0493(2004)132<1917:AARMMI>2.0.CO;2.

Wilks, D. S., 2011: *Statistical Methods in the Atmospheric Sciences*, Vol. 100. Academic press.

Williams, M., and R. A. Houze, 1987: Satellite-Observed Characteristics of Winter Monsoon Cloud Clusters. *Mon. Wea. Rev.*, **115 (2)**, 505 – 519, doi:10.1175/1520-0493(1987)115<0505:SOCOWM>2.0.CO;2.

Yamada, H., K. Yoneyama, M. Katsumata, and R. Shirooka, 2010: Observations of a Super Cloud Cluster Accompanied by Synoptic-Scale Eastward-Propagating Precipitating Systems over the Indian Ocean. *J. Atmos. Sci.*, **67 (5)**, 1456 – 1473, doi:10.1175/2009JAS3151.1.

Yang, G.-Y., and J. Slingo, 2001: The Diurnal Cycle in the Tropics. *Mon. Wea. Rev.*, **129 (4)**, 784–801, doi:10.1175/1520-0493(2001)129<0784:TDCITT>2.0.CO;2.

Yokoi, S., S. Mori, M. Katsumata, B. Geng, K. Yasunaga, F. Syamsudin, N. , and K. Yoneyama, 2017: Diurnal Cycle of Precipitation Observed in the Western Coastal Area of Sumatra Island: Offshore Preconditioning by Gravity Waves. *Mon. Wea. Rev.*, **145 (9)**, 3745–3761, doi:10.1175/MWR-D-16-0468.1.

Yu, H., R. H. Johnson, P. E. Ciesielski, and H.-C. Kuo, 2018: Observation of Quasi-2-Day Convective Disturbances in the Equatorial Indian Ocean during DYNAMO. *J. Atmos. Sci.*, **75 (9)**, 2867 – 2888, doi:10.1175/JAS-D-17-0351.1.

Yu, H., K. L. Rasmussen, and H.-C. Kuo, 2021: Quasi-2-Day and Diurnal Cloud Variation Timescales Over Convectively Active Regions. *J. Geophys. Res. Atmos.*, **126 (21)**, e2021JD035 426, doi:https://doi.org/10.1029/2021JD035426.

LIST OF TABLES

TABLE 1. CSPP-Geo Geocat dynamic ancillary data.

Dynamic ancillary data	**Data source**
Daily sea surface temperature data	Optimal Interpolated Sea Surface Temperature (Reynolds et al. 2007; Banzon et al. 2016)
Numerical Weather Prediction profiles	Global Forecast System (NCEP 2007)
Snow	NOAA Daily 4km Snow and Ice (National Ice Center 2008; Fetterer et al. 2015)

TABLE 2. Threshold used to filter the Level-1 and Level-2 products derived of Himawari-8 AHI.

Cloud property	**Threshold**
Cloud mask probability	≤1.0
Cloud optical depth	≤0.5
Cloud top temperature	≥300 K
Cloud top height	≤200 m

LIST OF FIGURES

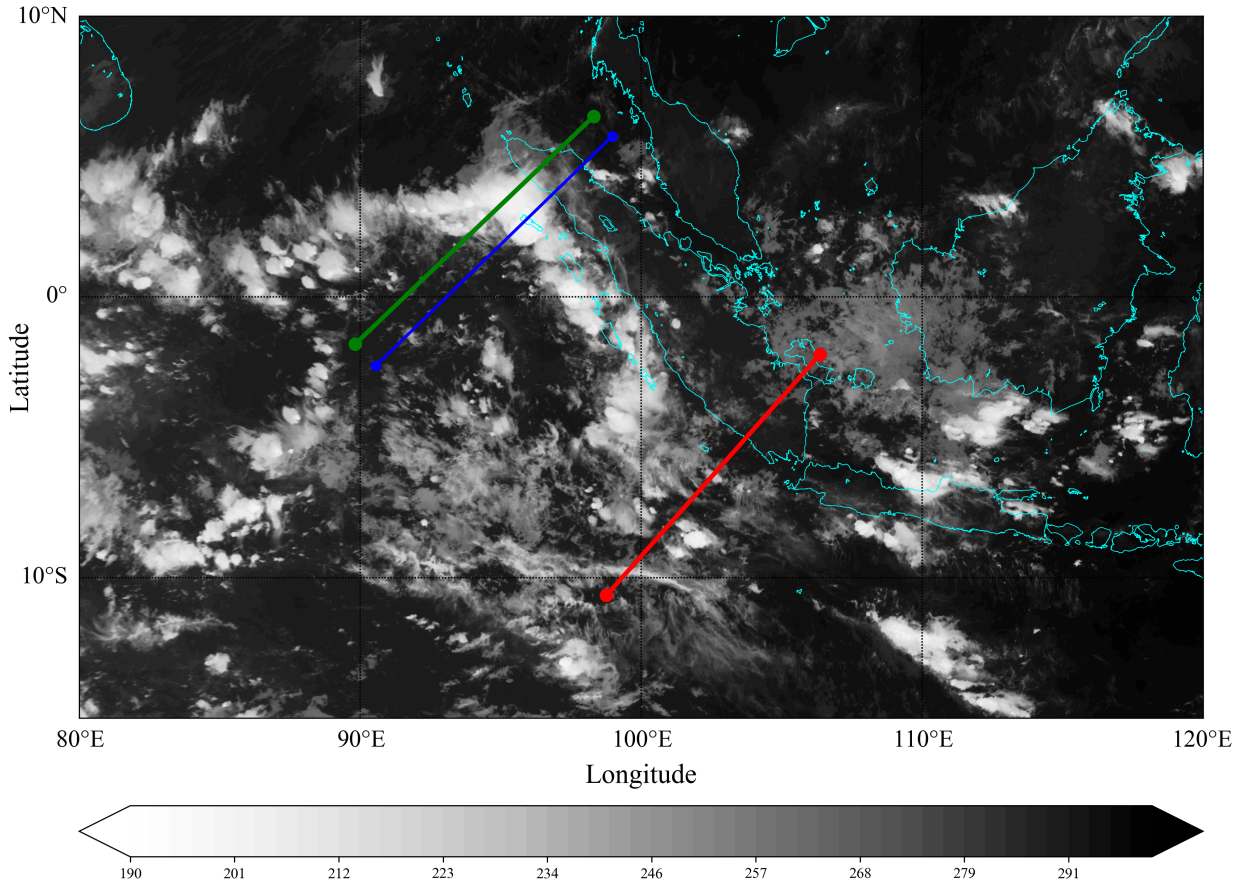

1031 FIG. 1. Himawari-8 AHI brightness temperature (K) of band 13 (10.4 μm spectral band) during the squall
1032 line propagation offshore Sumatra at 07:00 LST 11 January 2016. Perpendicular sections to the west coast of
1033 Sumatra are indicated; North in the green and blue lines, and South in the red line.

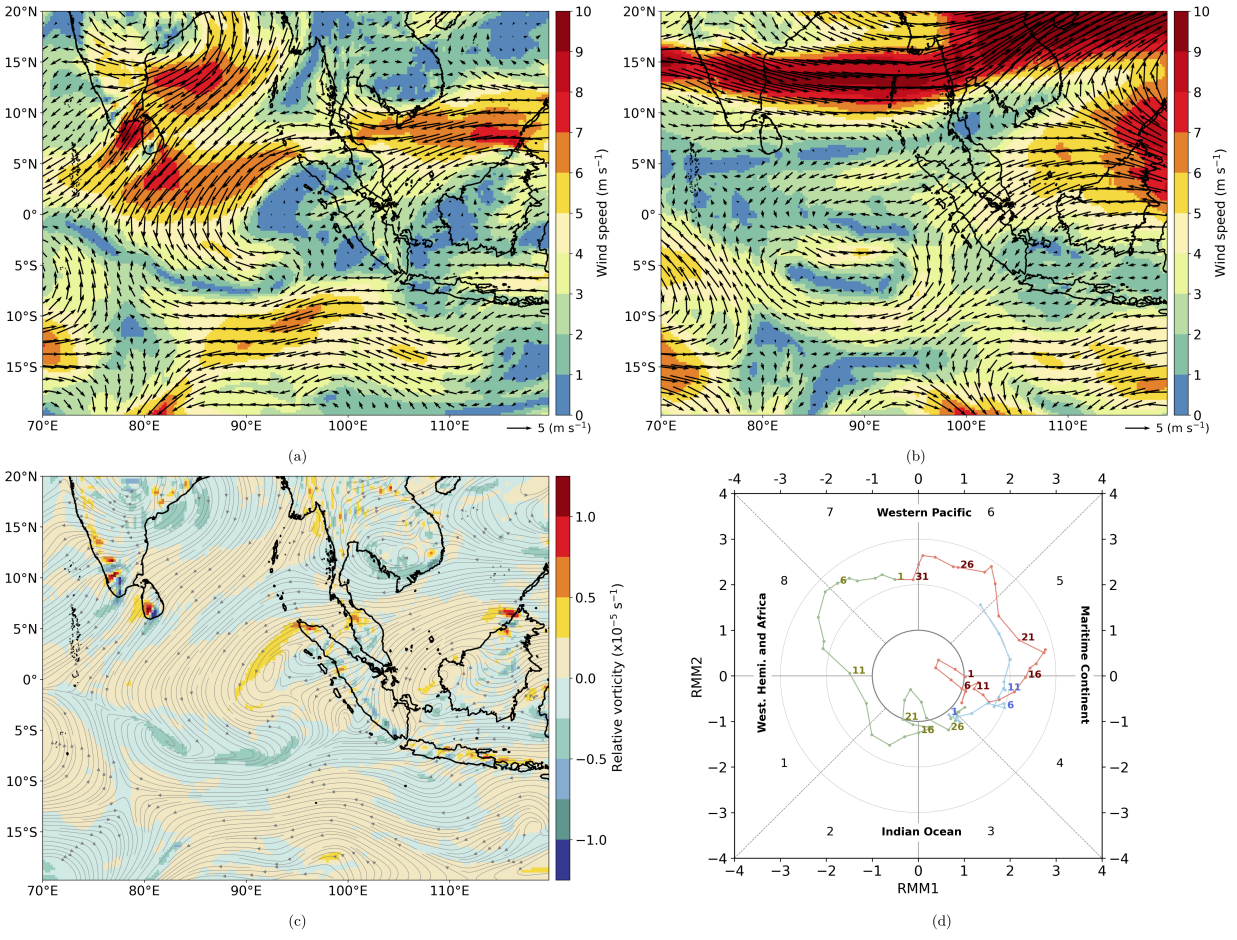

1034 FIG. 2. Wind vectors and wind speed (shaded, m s^{-1}) over the Indian Ocean and the Maritime Continent from
1035 ERA5; (a) Mean 925–850 hPa, and (b) 700 hPa. (c) Mean 925–850 hPa streamlines and relative vorticity (shaded,
1036 x10^{-5} s^{-1}) during the squall line event (10 January 2016-12 January 2016). (d) MJO indices from Wheeler-Hendon
1037 method during the austral summer 2015/16. December in the red line, January in the green line, and February in
1038 the blue line. Lines indicate the transit of the MJO through the Maritime Continent (Wheeler and Hendon 2004).

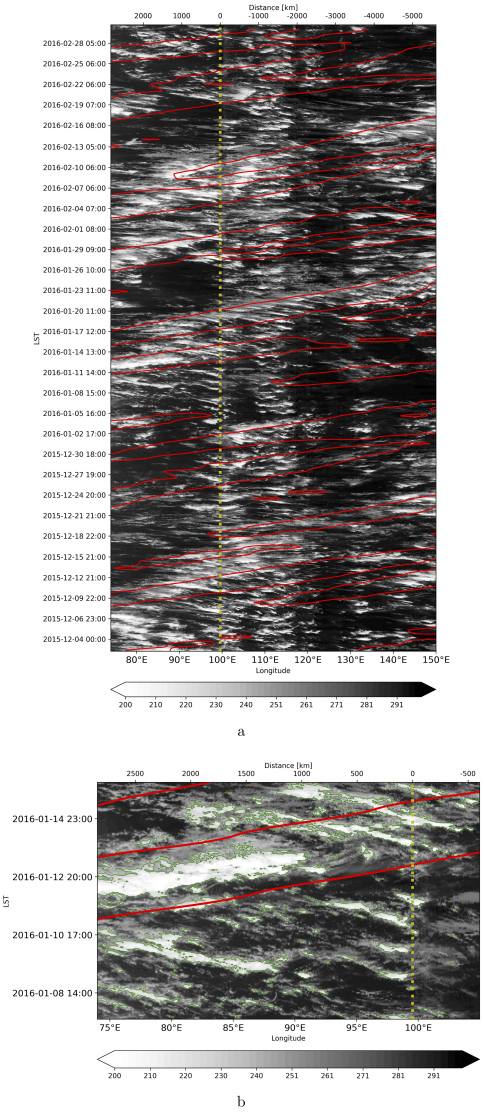

FIG. 3. Hovmöller diagram from Himawari-8 AHI brightness temperature (K) of band 13 (10.4 μm spectral band) and the Kelvin wave wavenumber-frequency filtered OLR (W m^{-2}), (a) austral summer DJF 2015/16, MJO is in its active phase over the MC in December 2015 and February 2016 (shaded contours). Kelvin wave propagated in January 2016 (red contour line), and (b) BT (K) during the squall line propagation offshore Sumatra over the Indian Ocean, staring. Deep convective regions are identified by 233(K) of BT of band 13 (green contour line). Red contours indicate the phase propagation of the Kelvin wave mode using global OLR (W m^{-2}) (Contour -5) along the equator from 74°E to 150°E. The yellow dotted line shows the position of the West Coast of Sumatra. 10 January 2016.

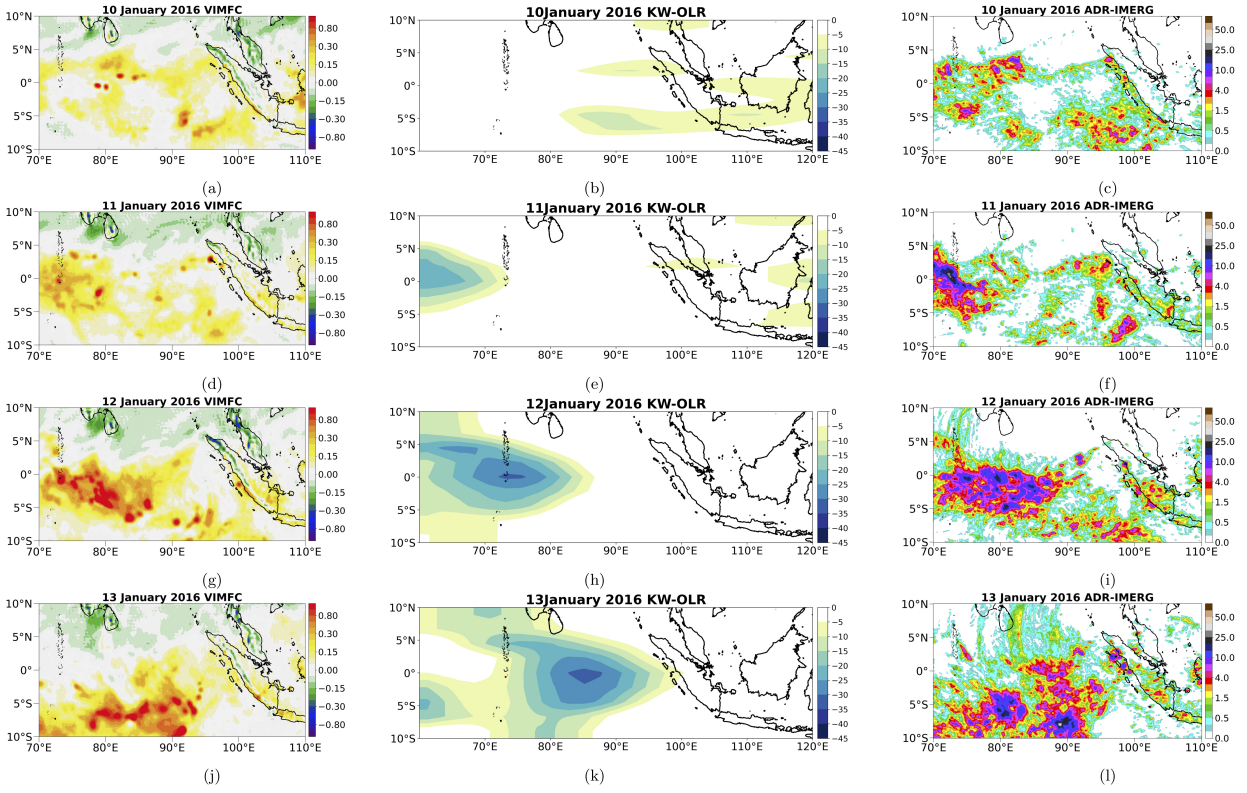

1047 FIG. 4. Eastward-propagating disturbances over the Indian Ocean. (a,d,g,i)Vertically integrated moisture flux
1048 convergence (VIMFC, (m s^{-1})(g kg^{-1})) from ERA5, (b,e,h,k) Kelvin wave wavenumber-frequency filtered OLR
1049 (KW-OLR, W m^{-2}), and (c,f,i,l) accumulated daily rainfall from IMERG (ADR-IMERG, mm hr^{-1}) for 10-13
1050 January 2016

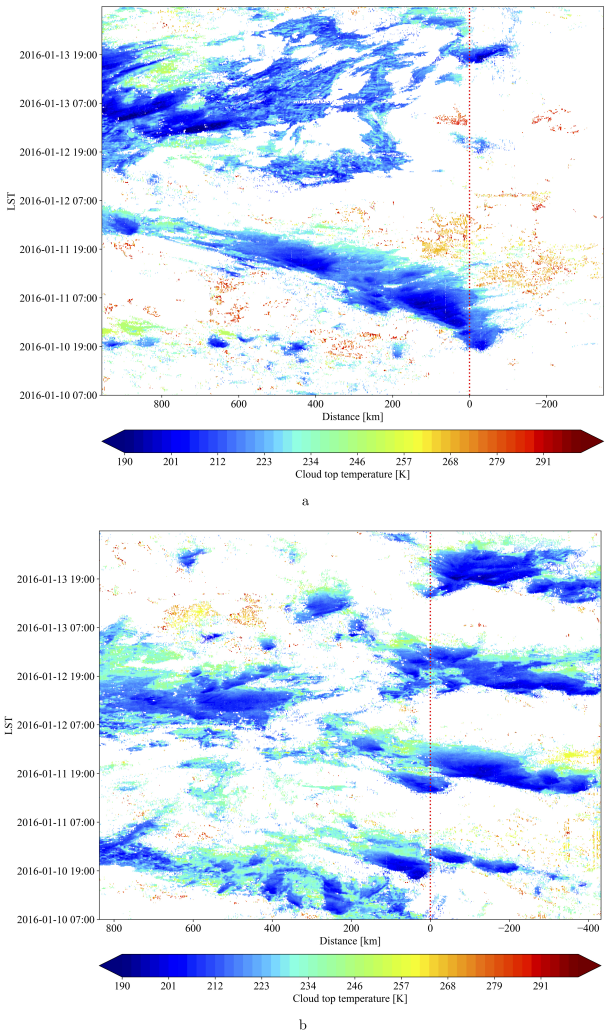

1051 FIG. 5. Hovmöller diagram of cloud top temperature (K) from Himawari-8 AHI between 07:00 LST 10 January
1052 2016 to 06:00 LST 14 January 2016 (shaded contours). (a) section North of Sumatra (green line in Figure 1),
1053 and (b)section South of Sumatra (red line in Figure 1). The red dotted line indicates the position of the West
1054 Coast of Sumatra.

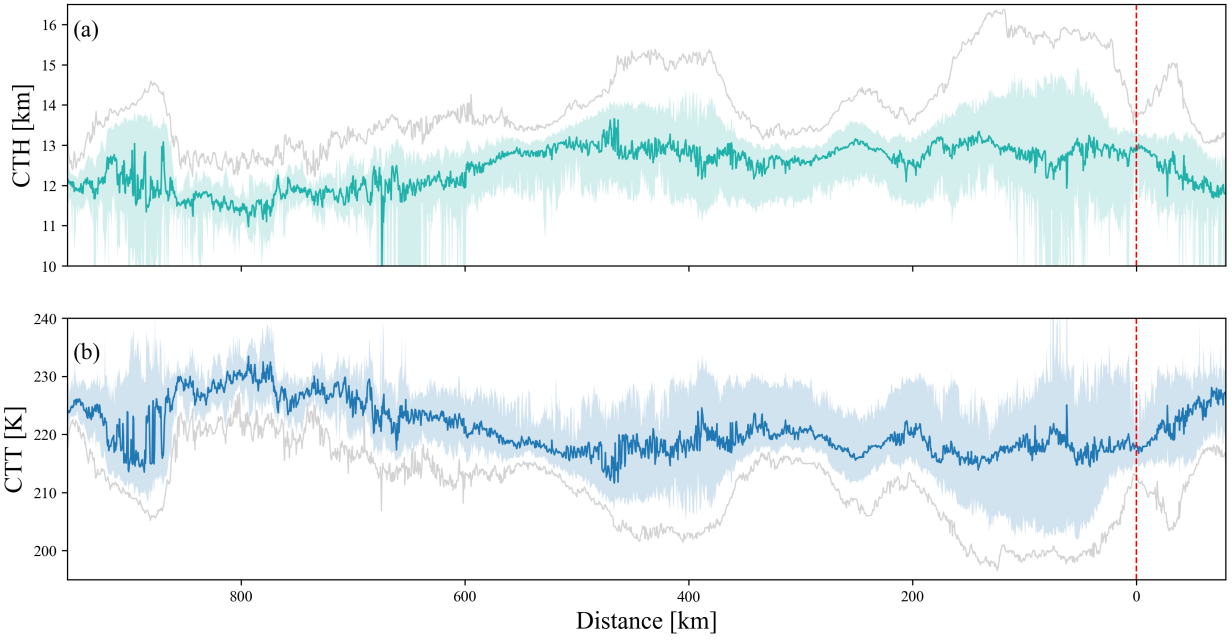

FIG. 6. Cloud properties from Himawari-8 AHI along to the section North in Sumatra (green line in Figure 1), from 17:00 LST 10 January 2016 to 07:00 LST 12 January 2016. (a) Cloud top height (CTH), the solid grey line indicates the 90th percentile and (b) Cloud top temperature (CTT), the solid grey line indicates the 10th percentile. Note that the solid cyan and blue lines indicate the 50th percentile, and the light and shaded areas show the interquartile range, and the red dotted lines show the position of the West Coast of Sumatra.

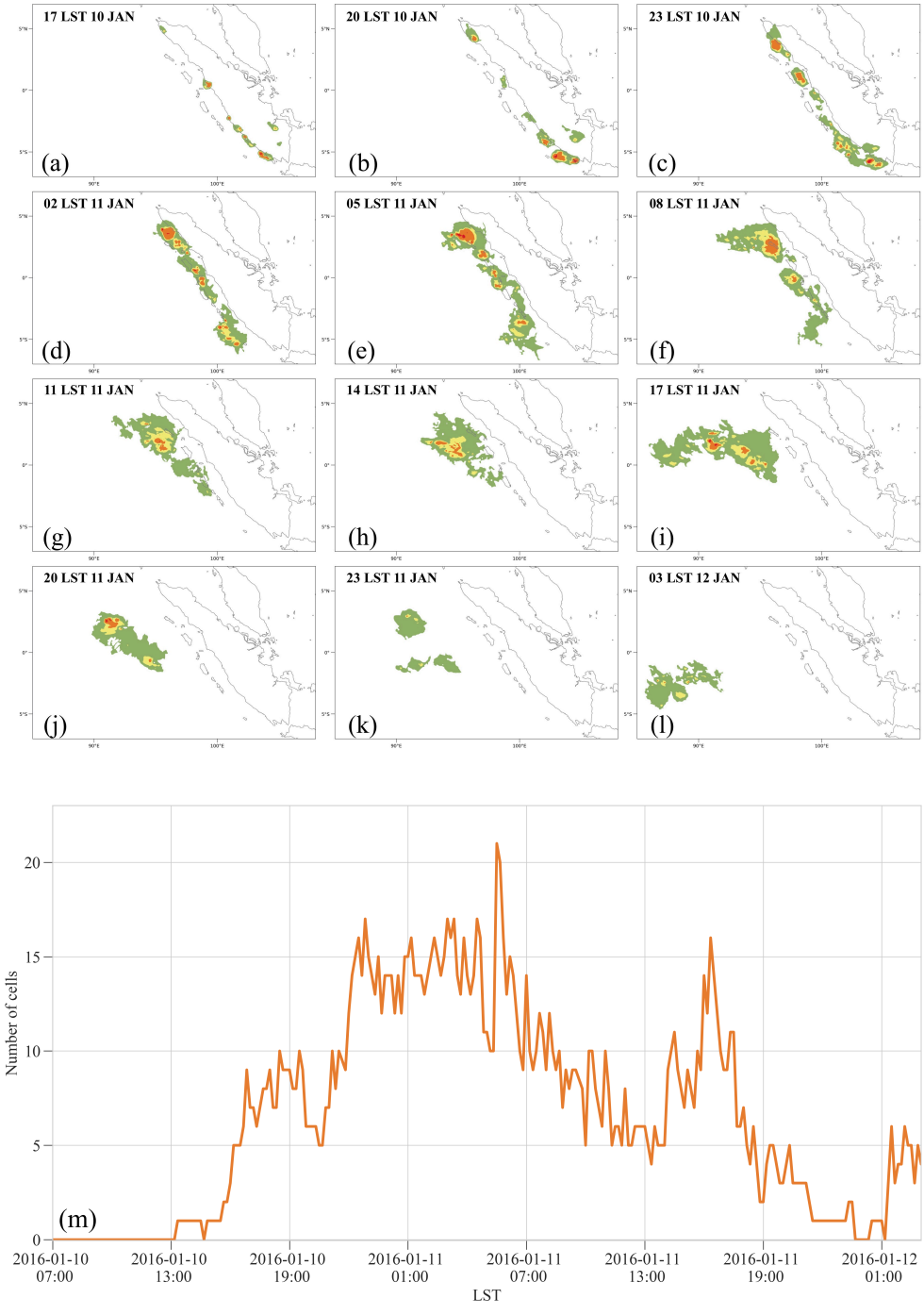

1060 FIG. 7. Cold convective cores are presented every 3 hours during the development of the tropical squall line
1061 based on the 10.4 μm spectral band from Himawari-8 AHI. Thresholds: 240 K in green, 213 K in yellow, 207 K
1062 in orange, and 195 K in red). Panel (m) shows the number of cells (10 min temporal-resolution) of cold cloud
1063 cores from 07:00 LST 10 January 2016 to 03:00 LST 12 January 2016.

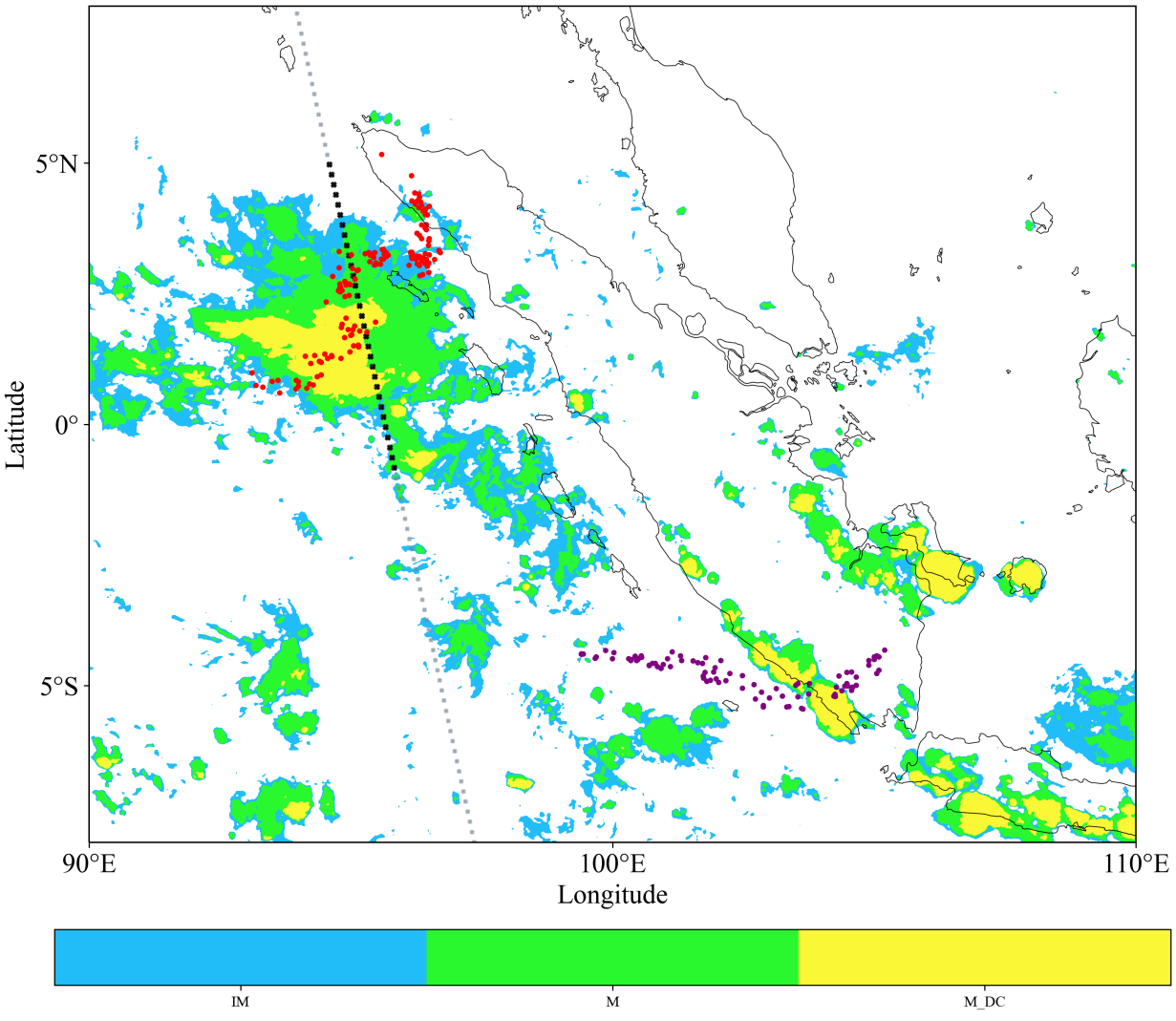

FIG. 8. The map shows an example of a convective mask derived from Himawari-8 AHI at 14:20 LST 11 January 2016. IM: Immature (blue shading), M: Mature (green shading), and M_DC: Mature and deep convection (yellow shading). The trajectories of the convective cells from the cell-tracking algorithm when the squall line propagates offshore Sumatra are indicated; North in the red dots, and South in the purple dots, and the ground path for the near-polar orbiting of the CloudSat satellite at 14:25 LST 11 January 2016 is showed in the grey dotted line, the section analyzed is indicated by the black dotted line.

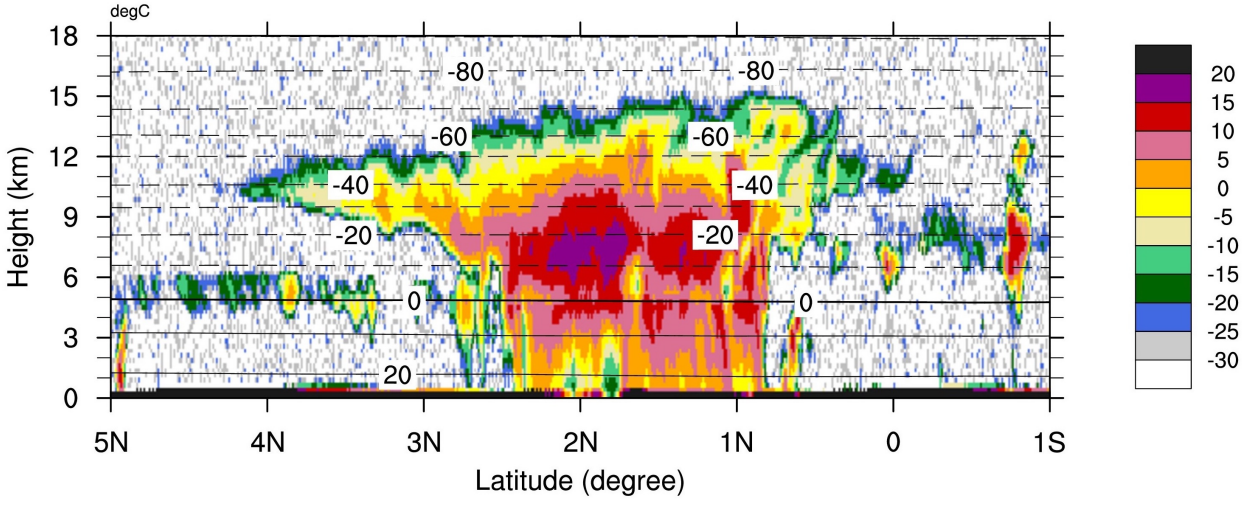

1070 FIG. 9. Vertical cross-section of the reflectivity (shaded, dBZ) from a CloudSat overpass through the squall
1071 line at 14:25 LST 11 January 2016 (black dotted line in Figure 8), and isotherms (°C).

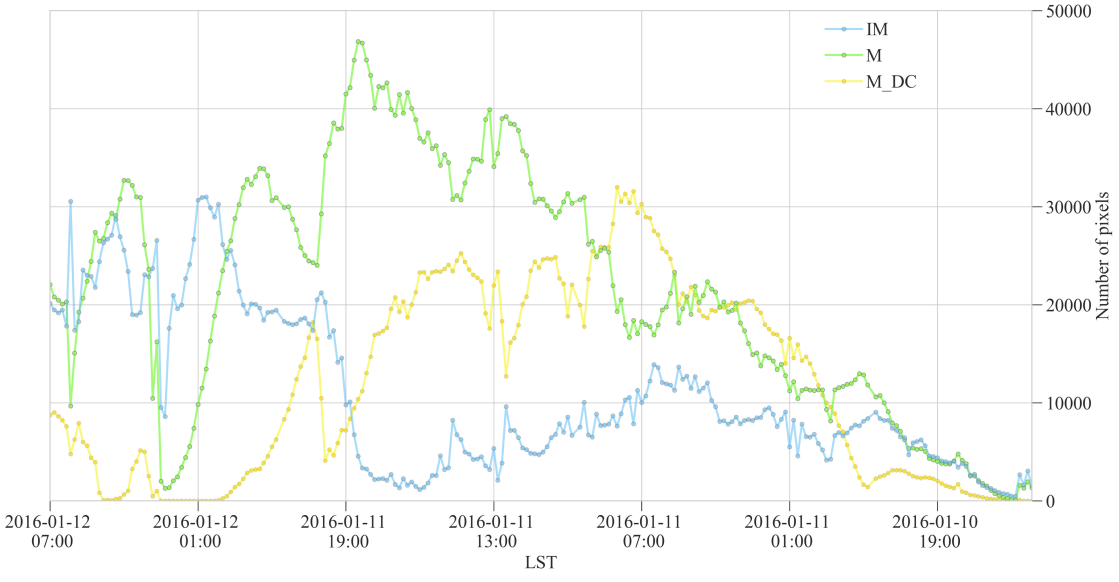

a

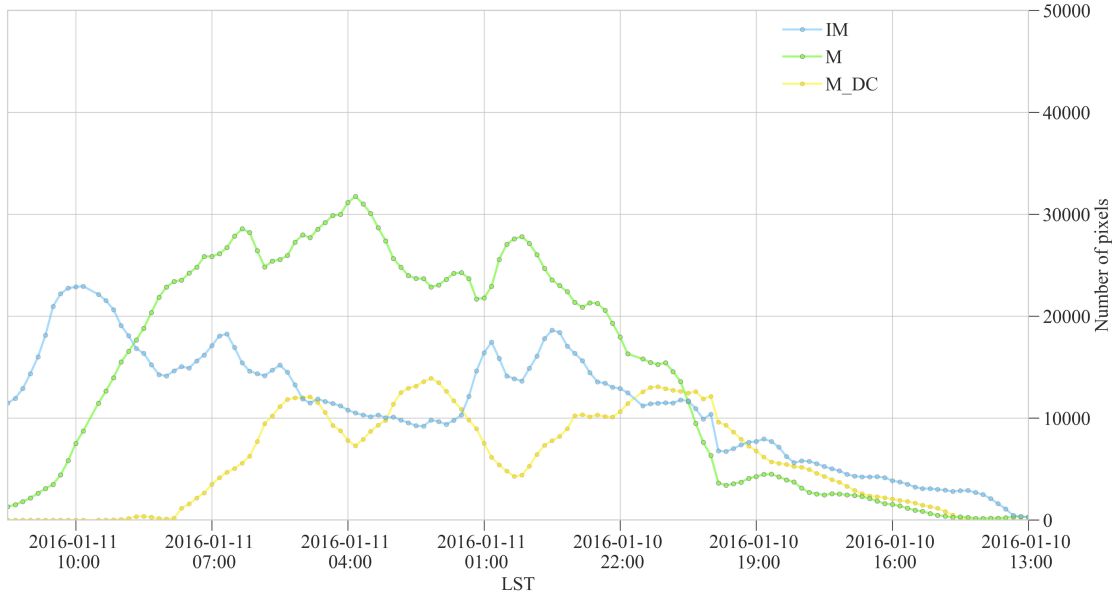

b

FIG. 10. Convective mask derived from Himawari-8 AHI, the x-axis represents the time during the propagation of the squall line off Sumatra, and the y-axis indicates the number of pixels in each position during the cell-tracking. IM: Immature (blue line), M: Mature (green line), and M_DC: Mature and deep convection (yellow line). (a) along the path of the storm in North of Sumatra, and (b) along the path of the storm in South of Sumatra. Note that x-axis in (a) and (b) are different.

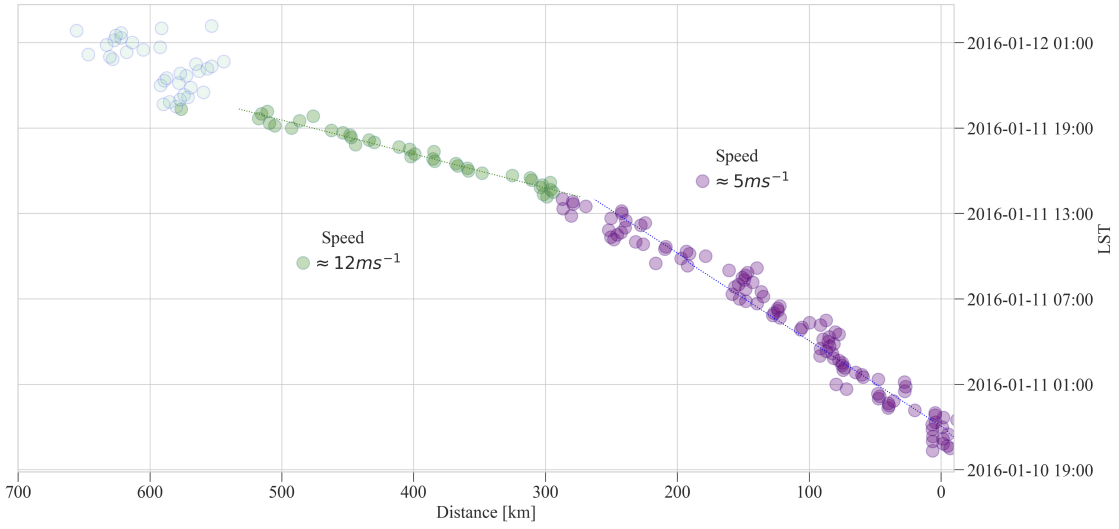

a

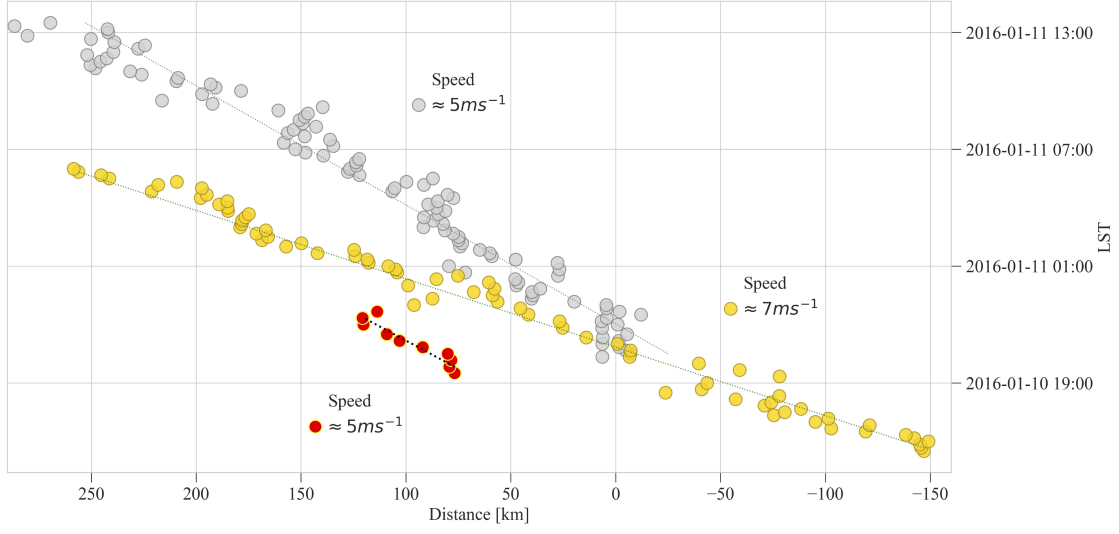

b

1077 FIG. 11. The Time-distance diagram shows the relative positions of the convective cells to the West Coast of
1078 Sumatra. The x-axis represents the distance in kilometers, and the y-axis indicates time. The dots are derived
1079 from the brightness temperature channel 13 and convective mask. (a) The dots indicate the relative position in
1080 the northwest of Sumatra. Speeds: 0-300: 5 m s^{-1}, 300-650: ~12 m s^{-1}, and (b) region South of Sumatra. Speeds:
1081 Inland: ~7 m s^{-1} (yellow dots) associated with the diurnal cycle from the East Coast, Ocean: ~5m s^{-1} (red dots)
1082 indicates the diurnal cycle from the East Coast. The signature of the diurnal cycles is superimposed off Sumatra,
1083 and grey dots indicate the first component in North of Sumatra. The dotted lines indicate the trend line in all
1084 cases.

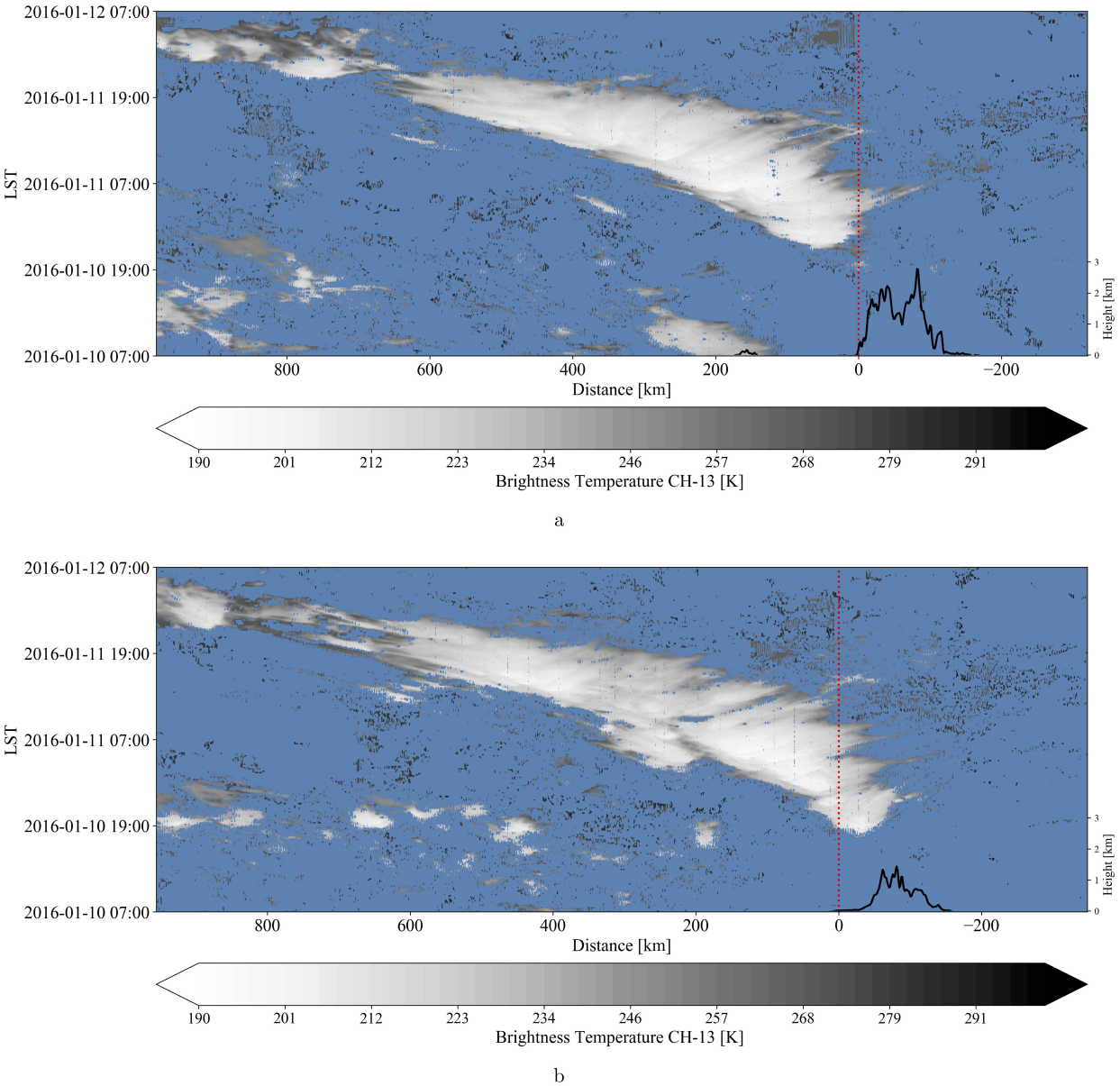

Fig. 12. Hovmöller diagrams filtered brightness temperature (K) of band 13 (10.4 μm spectral band) from Himawari-8 AHI between 07:00 LST 10 January 2016 to 19:00 LST 12 January 2016. (a) the proximity of the mountain ridge to the coastline in section North modulates the deep convective cell location over the northwestern of Sumatra(green line in Figure 1). The solid black line indicates topography height, and (b) mountains are located at 50 (km) from the West Coast of Sumatra (blue line in Figure 1). The red dotted line shows the position of the West coast of Sumatra.